

Precision Phase Shift Spectroscopy of Thallium

by
Toby E. Schneider

Prof. Protik K. Majumder, Advisor

A thesis submitted in partial fulfillment
of the requirements for the
Degree of Bachelor of Arts with Honors
in Physics

WILLIAMS COLLEGE
Williamstown, Massachusetts
September 9, 2007

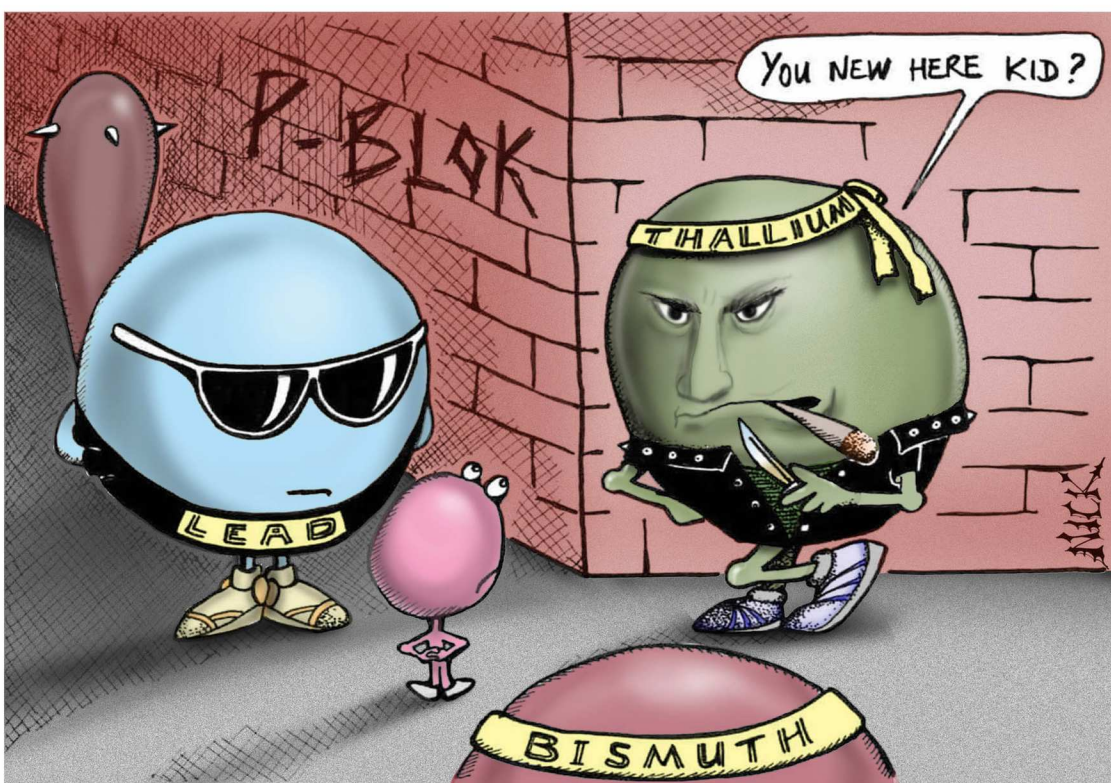
Acknowledgments

Many thanks to Tiku Majumder for all his excellent advice and friendship. I also greatly appreciate the technical expertise Larry Mattison and Emile Ouellete have given me. Thanks to the Williams Physics department for providing a great education and the best snacks at Williams. Also, thanks to my family and my friends for their moral support and comradeship throughout this endeavor.

Finally, I would like to dedicate this thesis to the future generations of thesis students who will strive to bring this work to its final fruition. I urge the reader of this thesis to contact me (electronic mail: 07tes@williams.edu) with any questions or further details desired.

Abstract

A method to perform precise spectroscopy using a differential phase shift technique in a novel Fabry-Perot ring cavity is presented. Studies of the Stark shift and the isotope shift for the thallium $6P_{1/2} \rightarrow 6P_{3/2}$ magnetic dipole transition are proposed. Substantial technical work has been accomplished to augment and improve the experimental system for the purpose of measuring these effects. A technique for accurately calibrating the frequency of atomic scans is developed. This thesis is another step in the long term goal of measuring a possible fundamental symmetry violation (a T-odd P-even force) in thallium proposed by Kozlov [Koz89].



Unwittingly, and against his mother's advice, Vince the first-row transition metal had been lured far away from home, and now found himself surrounded by heavier elements of the P-block.

Figure 1: Cartoon by Nick D. Kim, nearingzero.net. Used by permission.

Contents

1	Background	1
1.1	Symmetry Violation	1
1.2	TOPE Experiment	2
1.3	Present Contributions	3
2	Relevant Atomic Physics	5
2.1	$6P_{1/2} \rightarrow 6P_{3/2}$ transition in Thallium	5
2.2	Isotope Shift	7
2.3	Stark Shift	8
2.4	Phase Shift Spectroscopy	8
3	Experimental Techniques and Implementation	11
3.1	Differential Signal Method	11
3.2	Optics	13
3.3	Fabry-Perot Ring Cavity	17
3.4	Atomic Beam Apparatus	17
3.5	Cavity Locking	17
3.6	Summing Amplifier	20
3.7	Exploiting Faraday Rotation for Laser Stabilization	22
4	System Performance	25
4.1	Stability of Optics	25
4.2	Laser Scanning	25
4.3	Differential Signal	26
4.3.1	Noise with Laser Unlocked	28
4.3.2	Noise with Scanning Laser	29
4.3.3	Differential Signal over Long Scans	29
4.4	Quality of Laser Lock System	30
5	Calibrating Laser Scans	33
5.1	Airy Functions	33
5.2	Exploiting the Airy Function for Calibration	34

6	Future Work	39
6.1	Conclusions	39
6.2	Detecting and Optimizing the Experimental Signal	39
6.3	Isotope Shift Measurement	41
6.4	Stark Shift Measurement	41
6.5	TOPE Experiment	42
A	Ring Cavity Locking Hardware	43
A.1	Scanning the Laser Frequency	43
A.2	Hardware	44
B	Laser Locking Hardware	47
B.1	System Improvements	47
B.1.1	Oven	47
B.1.2	Faraday Rotator	52
B.1.3	SRS SIM 960 PID Controller	52
B.2	Laser Locking Procedure	53
C	Laser Scan Calibration: Technical Details	55
C.1	Data Preprocessing	55
C.2	Airy Function Fitting	57
D	Acquisition and Control Software	61
D.1	A Graphical Programming Language	61
D.2	Data Acquisition with the NI-DAQ PCI 6221	63
D.3	Analog Input Monitor	64
D.4	Analog Data Collection with Smooth AO Scanning	64
D.5	Stepper Motor Control	65
D.6	Oscilloscope Networking	67

List of Figures

1	Cartoon by Nick D. Kim, nearingzero.net. Used by permission.	iv
2.1	Valence energy level structure showing fine and hyperfine structure for ^{203}Tl and ^{205}Tl . Adapted from [Ker05].	6
3.1	Simulation of ideal common mode noise rejection. Signals 1 and 2 originate from the same source and experience the same environment.	12
3.2	Simulation of the output of the Fabry-Perot ring cavity demonstrating the frequency shifting of one beam. In (a), both beams are the same frequency. In (b) one beam is shifted by exactly one free spectral range. The boxed portion of (b) corresponds to figure 3.3 (a).	13
3.3	Simulation of the differential signal. (a) shows the output of the ring cavity when both beams are off resonance with the atomic transition. The differential signal (c) is measured from the lock point shown. (b) illustrates the two signals when one is on resonance. The expected differential signal for a single peak is shown in (c), which is adapted from models done by Butts in [But06]. A single beam interacting with the atomic transition leads to a differential signal that is the derivative of a dispersion curve. As both beams interact with the atomic transition during the scan, two of these dispersion derivative lineshapes are present.	14
3.4	Schematic of Experimental Apparatus including the general layout. Some details have been omitted or modified for clarity.	15
3.5	Photograph of the Fabry-Perot ring cavity.	18
3.6	Rendered model of the Fabry-Perot ring cavity with counterpropagating laser beams interacting perpendicularly with the atomic beam. The actual ring cavity structure is not shown, only the mirrors. Note the cavity shield which was added to protect the mirrors from stray thallium.	19
3.7	Voltage Divider to attenuate PID output to prevent overdriving off the lock system.	20
3.8	Electrical Schematic of a Summing Amplifier for the Cavity Lock System. Note that both preamplifiers are inverting as is the summing amplifier, thus yielding an output that is directly proportional to the sum of both inputs (not negative) as desired.	22
3.9	Diagram of the polarimeter setup for the laser locking system.	23

4.1	Laser output after fiber output coupler as a function of frequency. . .	26
4.2	Demonstration of minimizing noise on the differential signal by aligning CW (unshifted, yellow) and CCW (frequency shifted, blue) output signals. (a) demonstrates maximizing power on both beams. (b) demonstrates signal averaging both beams. Not shown is the final step of aligning both beams to match in amplitude and frequency. The undesired "miniature" peaks visible in (a) are due to imperfect mode matching within the ring cavity, and are reduced by good alignment.	27
4.3	Oscilloscope trace demonstrating the common mode noise rejection of the differential signal with the <i>laser unlocked but not scanning</i> . Note that the root-mean-square (RMS) of the signals are all similar, and the differential signal is shown ten times amplified. The Airy peak height for both shifted and unshifted beams is 550 mV. The ring cavity is locked using a PID controller time constant of 1 ms, and the differential signal amplifier was set to a bandwidth of 3 kHz.	28
4.4	Oscilloscope trace demonstrating the common mode noise rejection of the differential signal with the <i>laser scanning at 5 Hz</i> over 1 GHz around the 1283 nm (233612.7 GHz) transition. As in figure 4.3 the root-mean-square (RMS) of the signals are all similar, and the differential signal is shown ten times amplified. The Airy peak height for both shifted and unshifted beams is 550 mV. The ring cavity is locked with a PID time constant of 10 μ s.	29
4.5	Long range (>4 GHz) scan in the region of the 1283 nm transition. The CW (clockwise) beam is not frequency shifted, while the CCW (counterclockwise) beam is. Note that the drift over this region is about 14 times larger than the short term RMS noise (as seen in figure 4.3).	30
5.1	Airy functions of differing finesse.	34
5.2	Two simulations of Airy functions (left) a function of voltage (scaled as x) showing different forms of nonlinearity. (a) has a positive quadratic term and (b) has a negative quadratic and a small positive cubic term. The right is the corresponding graph of $\nu(x)$	35
5.3	Four calibration scans demonstrating the nonlinear relationship of voltage (rescaled to x) and frequency. Two of the scans (blue and green curves) start a low voltage and move to a higher one (up scans) and the other two scan the opposite direction (down scans). Hysteresis can be noticed upon close examination.	37
6.1	Configuration of the ring cavity necessary for the future Stark shift (a) and TOPE (b) experiments.	41

A.1	Laser Configuration: the laser diode emits a broad frequency spectrum from which a single frequency is selected for stimulated emission by the position of a PZT controlled diffraction grating.	43
A.2	ThorLabs AE0505D18 PZT used to replace the defective stack in the experiment's diode laser.	44
A.3	Final prototype of the Summing Amplifier.	45
A.4	Block Diagram of the present cavity locking system. Note: the values for the summing amplifier preamp coefficients: a can be tuned from 0.001 to 0.01 and b can be tuned from 5 to 10. This can be directly calculated from the resistors used in figure 3.8. Also, the laser and cavity PZTs are not physically connected to the photodetector; rather, they affect the laser frequency and cavity path length which in turn changes the signal on the photodetector.	46
B.1	Block Diagram of the laser locking system.	48
B.2	Basic parts of the Laser Locking Oven. Materials rendered transparent for ease of view.	49
B.3	Electrical circuitry for powering a clamshell heater elements. This circuitry is duplicated four times for all the heaters (N1, N2, S1, S2).	49
B.4	Diagram of connectors for heating element leads to external routing cable. Plates are aluminum (again shown transparent) and contacts are dry, as solder would melt in the oven environment.	50
B.5	Isometric view (a) and side view (b) of the vacuum tube end caps. Bolts tighten the two aluminum parts (shown transparent here) onto an O-ring to make a seal against the ceramic tube. Not shown is the connection to the vacuum pump (north cap) and thermocouple inputs (south cap).	51
B.6	Final prototype of the new water cooled solenoid and mount for creating an AC magnetic field in the polarimeter's glass rod.	53
C.1	Graphical demonstration of the peak location algorithm on actual data. a) shows the raw data and b) shows the data after rejecting values below the threshold.	59
C.2	Graphs provided to user by <i>Fit_Airy_Version1_1_07tes.m</i> to validate a successful prefit (a) and final fit (b).	60
D.1	Pinout of the NI-DAQ PCI-6221 card. AI is analog input, AO is analog output, <i>Pport.line</i> is a digital line configurable in software as input or output. [Nat05]	62
D.2	Front panel (user interface) of the <i>LaserSmoothScanv2.1.vi</i> smooth scanning data collection routine.	66

Chapter 1

Background

Physics is a delightfully diverse discipline that has a common thread: the search for how the universe works. Aiming to fulfill this goal in one small way, this lab eventually wishes to push the limits of the Standard Model for electroweak force interactions and along the way help theorists better realize their models for heavy (and therefore complex to model) atoms. Both of these goals, however, require thoughtful and extensive application of technology: from computers, oscilloscopes, lasers and optics to vacuum systems and ovens. It is here, in the engineering and optimization of the experimental system, that this present work is focused. Before turning to those details, some background on the physics of interest is in order.

1.1 Symmetry Violation

Symmetry, in the macroscopic regime, is such an ingrained element of our world view and the basis of physics that the idea of symmetry violation is difficult to grasp. Physicists have believed and continue to believe that the laws of the universe are invariant under a change of place, time or rotation. If Albert drops a ball on Earth and Blaise drops one on Mars, the physical laws (momentum and energy conservation) governing the motion of both balls are the same. If Erwin performs an experiment multiple times, he expects the physical laws to remain constant from one to the next. Since nothing has caused us to doubt that these continuous symmetries (location, time, rotation) hold, we are able to make meaningful progress in the natural sciences.

Modern physics, notably quantum mechanics, has taught us that our macroscopic notions did not necessarily hold in the realm of the very small. Fundamental particles do not act like billiard balls as one might first suppose. Particle interactions obey (conserve) or break (violate) a set of discrete symmetries: parity (P), time reversal (T), and charge conjugation (C). The traditional assumption of symmetry conservation is that particles will interact in the same way if any of these parameters are reversed. Parity conservation says that the interaction between particles with a coordinate system (x,y,z) is mathematically equivalent to the interaction with the inverted coordinate system $(-x,-y,-z)$. Conservation of time reversal symmetry requires that a

process is the same whether or not time runs forward. While it is currently impossible to reverse time, it is possible to gain insight into this symmetry by reversing the direction of all time-relevant processes in an interaction. For example, a laser beam is time dependent as the light starts in the laser and moves in space as a function of time. A time independent example is two charged plates which cause an electric field that does not depend on time. Finally, charge symmetry states that an interaction follows the same physical laws when all the particles are replaced with anti-particles and vice-versa.

Until the middle of the last century, physicists assumed these three discrete symmetries held in fundamental particles. After all, symmetry conservation permeates our lives and thus our thinking. However, this changed when Dr. Wu at Columbia University collaborated with Dr. Ambler et al at the National Bureau of Standards to perform experiments (published in 1957 [WA57]) conclusively demonstrating parity violation (parity non conservation or PNC) in the beta decay of ^{60}Co . Their work was prompted by theory work by Drs. Lee and Yang in 1956 [LY56]. This is an excellent example of symbiosis between theory and experiment, where both approaches work to improve the results of the other.

Based on fundamental assumptions, the Standard Model of Electroweak interactions presently has provisions for non-conservation in the form of the CPT theorem. Only the weak force has been demonstrated to violate parity, the other fundamental forces (gravitational, strong and electromagnetic) do not. Furthermore, the CPT theorem states that for any system, the product of the symmetries is conserved. Thus, if CP-violation exists, which it does, one can infer T-violation. Finding such a time-reversal violation, or putting a precise bound on its existence, is one of the goals of this work.

1.2 TOPE Experiment

No experiments have yet put a stringent limit on the size of a possible time-reversal violating while parity conserving (T-odd / P-even or TOPE) force, an interaction which is not directly predicted by the Standard Model. Consider a spectroscopic interaction between a laser beam and an atom in an electric field that is parallel to the laser's direction of propagation. A component of the Hamiltonian is then

$$\hat{k} \cdot \vec{E} \tag{1.1}$$

where \hat{k} is the propagation vector of the laser and \vec{E} is the electric field. Applying a time-reversal operator T to equation 1.1 yields

$$T(\hat{k} \cdot \vec{E}) = -\hat{k} \cdot \vec{E} \tag{1.2}$$

since the direction of \hat{k} reverses when time does, but the electric field is unvarying. Therefore, reversing the direction of the laser in the interaction is equivalent to reversing the time. For further details regarding this measurement, refer to chapter 4

of [Ker05]. The desire to measure this effect precisely has informed the design of a unique Fabry-Perot ring cavity, where two individual beams interact with the atoms in the same conditions but in the opposite directions, as discussed later in this thesis.

1.3 Present Contributions

Due to the speculative nature of the TOPE experiment, it is useful first to test the performance of the experimental system on several other measurements outlined in the next chapter that are based on known effects. These measurements of the Stark shift and isotope shift in thallium are useful in their own right, as well as providing a useful first test of the apparatus developed in this lab.

This work is a long term project, and a number of the steps accomplished recently during the author's time in the laboratory over the past year are outlined in this thesis. Many of the contributions are technical: strides were made to upgrade, improve and repair the experimental apparatus. The design of the system (a mixture of past and present work) is given in chapter 3, and specific modifications are detailed in appendices A and B. The ensuing performance, after this technical work, is discussed in chapter 4. Furthermore, a technique (chapter 5) and implementation (appendix C) for calibrating the frequency of the laser were developed. This is a critical aspect towards accurately interpreting future atomic data. Finally, a computer upgrade was completed, and numerous new software programs were written for data collection and control of laboratory equipment, as discussed in appendix D.

The next chapter outlines the basics of atomic physics relevant to the techniques employed in this lab and to the measurements that will be made in the future.

Chapter 2

Relevant Atomic Physics

2.1 $6P_{1/2} \rightarrow 6P_{3/2}$ transition in Thallium

Thallium, beyond its dubious distinction as a highly toxic poison causing hair loss and death, is an element that has little interest to the general public. However, it is an excellent candidate for parity non-conservation (PNC) work because of the large size of the nucleus ($Z = 81$), since PNC effects scale approximately as the cube of the atomic number (Z^3). This means that the amplitude of these effects in thallium is over five orders of magnitude greater than in hydrogen, the simplest and best understood element. Heavy atoms like thallium are also much more complex to model theoretically, leading to a need for experimental verification of wavefunctions derived from first principles. Through a symbiosis of experiment and theoretical work, greater precision can be placed on fundamental electroweak forces. The weak charge (Q_W) is related to the experimentally measured PNC effect (ϵ_{PNC}) and the theoretically derived $C(Z)$ by

$$\epsilon_{PNC} = Q_W \cdot C(Z) \quad (2.1)$$

Thus, precise determination of Q_W requires both theoretical modeling work and spectroscopic experiments, the latter of which this lab is pursuing. The spirit of this type of research, where both experiment and theory are necessary to put a stringent limit on the value under study, extends to the proposed TOPE force experiment and other searches in atoms.

In the ground state, thallium has the electronic configuration

$$[Tl] = [Xe]4f^{14}5d^{10}6s^26p^1 \quad (2.2)$$

where $[Xe]$ is the ground state electronic configuration of the noble gas Xenon. Thus, thallium can be viewed as a one electron P-valence system, as is done in this lab. The fine and hyperfine structure of the low-lying levels of thallium are shown (with rough values of the associated excitation energies) in figure 2.1 for both naturally occurring isotopes of thallium. These isotopes are ^{203}Tl and ^{205}Tl and occur in a ratio of $\sim 3:1$. The transition mediator (the electric or magnetic multipole) which is mandated by

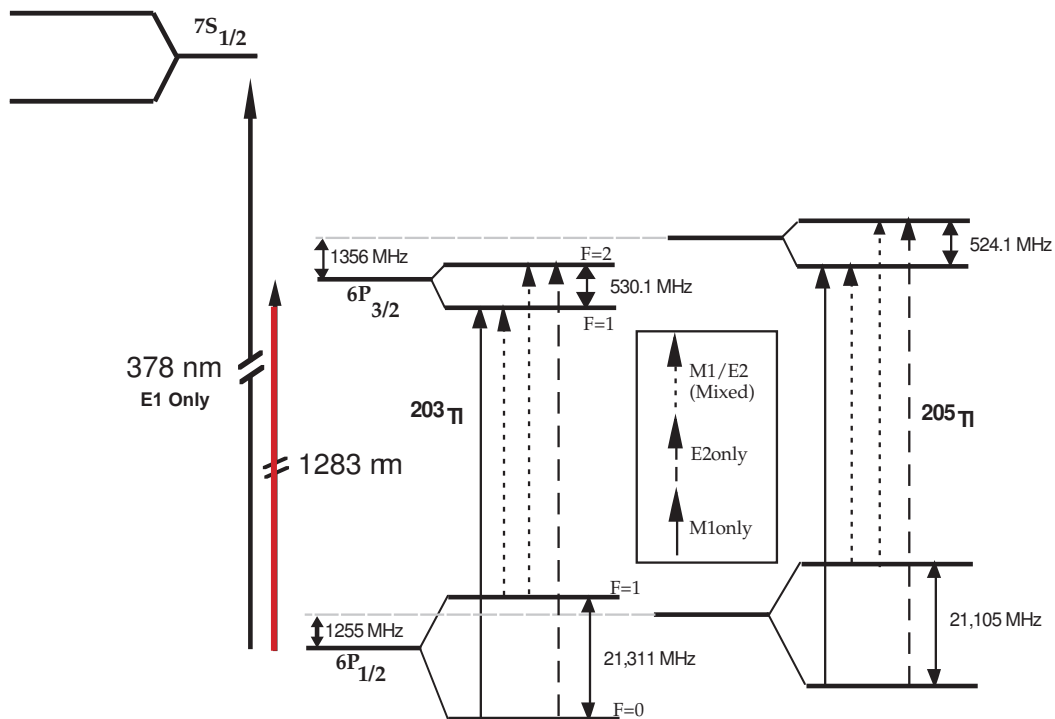


Figure 2.1: Valence energy level structure showing fine and hyperfine structure for ^{203}Tl and ^{205}Tl . Adapted from [Ker05].

the quantum mechanical selection rules for the possible transitions is also labeled. The electric dipole (E1) transition requires a change in parity ($\Delta l = \pm 1$); therefore, all of the transitions within the P -subshell are E1-forbidden while the $6P_{1/2} \rightarrow 7S_{1/2}$ is allowed. This transition between orbitals is excited by light at 378 nm and has been the subject of prior measurements in this lab, including a Stark shift value [Dor02] that matched recent theory based wavefunction calculations done by an independent group [SJSC06].

The excitation of interest in the current work is the $6P_{1/2} \rightarrow 6P_{3/2}$ transition (shown in red on 2.1). The selection rules dictate that the magnetic dipole (M1) and electric quadrupole (E2) can drive these transitions. Based on the selection rules governing the hyperfine splitting, $F = 0 \rightarrow F' = 1$ is an M1 transition, $F = 0 \rightarrow F' = 2$ is E2, and $F = 1 \rightarrow F' = 1, 2$ is both. The hyperfine splitting from both isotopes means eight distinct transitions in the 1283 nm region, located in two groups of four separated by the large hyperfine splitting (>21 GHz) between $F = 0$ and $F = 1$. Presently, the work is focused on the set of lines originated from the $F = 1$ ground state. The techniques can easily be extended to the $F = 0$ ground state, which will be of interest for the TOPE experiment ($F = 0 \rightarrow F' = 1$).

This transition has been historically of interest as the value of the PNC optical rotation for this 1283 nm $6P_{1/2} \rightarrow 6P_{3/2}$ transition was measured and reported in [VMM95]).

2.2 Isotope Shift

Testing and fully understanding the precision of the system is critical before attempting to measure the TOPE force, which quite possibly may not exist. To this end, two experiments are proposed as a first step. The first of which is to measure the isotope shift in the 1283 nm $6P_{1/2} \rightarrow 6P_{3/2}$ transition. The isotope shift is caused by the differing number of neutrons (^{203}Tl versus ^{205}Tl) in the nucleus. The difference in the nucleus causes a redistribution of charge and consequently a shift in the resonance frequency of atomic transitions, including those of the $6P_{1/2} \rightarrow 6P_{3/2}$ that this work is focused on. Generally speaking, this is caused by the fact that even valence electron wavefunctions interact with the nucleus; thus, the composition of the nucleus affects the electronic structure. For this transition, the isotope shift has been estimated to be ~ 100 MHz by taking the difference of the isotope shift measured in the $6P_{1/2} \rightarrow 7S_{1/2}$ and the $6P_{3/2} \rightarrow 7S_{1/2}$ transitions. No direct measurement has been made of this shift in the $6P_{1/2} \rightarrow 6P_{3/2}$ transition yet, and this is what this work aims to do in the near future. A precise measurement of this effect will help theorists test their models of the thallium nucleus, as it is a nuclear effect (the only difference between isotopes is in the nuclear mass and charge distribution).

2.3 Stark Shift

The Stark shift is simply a small shift in atomic energy levels in the presence of an external electric field. In thallium, the Stark effect is a second order perturbation described by a small potential

$$H' = \vec{d} \cdot \vec{E} \quad (2.3)$$

where \vec{E} is the electric field and \vec{d} is the dipole moment. The energy shift grows as the quadratic of the electric field and can be calculated from an infinite sum over all wavefunctions

$$\Delta\epsilon_{Stark} = \sum_{m \neq n} \frac{|\langle \Psi_m^0 | H' | \Psi_n^0 \rangle|^2}{\epsilon_n^0 - \epsilon_m^0} \quad (2.4)$$

Assuming the electric field lies in the \hat{z} direction (which is easy to accomplish experimentally), \vec{d} becomes ez and equation 2.4 simplifies to

$$\Delta\epsilon_{Stark} = E^2 \sum_{m \neq n} \frac{|\langle \Psi_m^0 | ez | \Psi_n^0 \rangle|^2}{\epsilon_n^0 - \epsilon_m^0} \quad (2.5)$$

Experimental measurements would typically quote a value for the Stark shift constant, k_{Stark} , which is equal to the frequency shift divided by the square of the electric field

$$k_{Stark} = \frac{\Delta\nu}{E^2} \quad (2.6)$$

$\Delta\nu$ can be measured and E can be calculated from the shape and charge of the electric field plates employed.

The motivation for measuring the Stark effect is to again provide verification for theorists modeling thallium from first principles. Since the Stark effect is calculated as a sum over all the atomic wavefunctions, it is a helpful verification of the validity of the theoretically derived wavefunctions. These verified wavefunctions can then be used in calculating more precise values for $C(Z)$ and thereby put constraints on the weak charge (see equation 2.1).

2.4 Phase Shift Spectroscopy

In a nonconducting, isotropic medium, it is possible to classically model the interaction between light and matter as a time dependent electric field (the electric component of light¹) interacting with classical damped harmonic oscillators (the bound electrons). The interaction of a laser beam and a cloud of thallium gas is such an interaction. The differential equation for this situation is thus

$$m\ddot{\mathbf{r}} + m\gamma\dot{\mathbf{r}} + K\mathbf{r} = -q\mathbf{E} \quad (2.7)$$

¹The magnetic component can safely be ignored as it is much smaller than the electric component of light.

where m is the electron mass, $m\gamma$ is a damping constant, K is the effective spring constant, \mathbf{r} is the displacement of the electron from rest, q is an elementary charge, and \mathbf{E} is the electric field of light ($\mathbf{E} = E_0 e^{i\omega t}$). Equation 2.7 solves to

$$\mathbf{r} = \frac{-q\mathbf{E}}{-m\omega^2 - i\omega m\gamma + K} \quad (2.8)$$

The macroscopic polarization (\mathbf{P}), the density of electric dipoles, is given by

$$\mathbf{P} = -Nq\mathbf{r} \quad (2.9)$$

where N is the number density of the medium. Substituting for the changing value of \mathbf{r} present in equation 2.8

$$\mathbf{P} = \frac{Nq^2\mathbf{E}}{-m\omega^2 - i\omega m\gamma + K} \quad (2.10)$$

Defining an effective resonance frequency ω_0 where

$$\omega_0 = \sqrt{\frac{K}{m}} \quad (2.11)$$

allows equation 2.10 to be rewritten as

$$\mathbf{P} = \frac{Nq^2\mathbf{E}/m}{\omega_0^2 - \omega^2 - i\omega\gamma} \quad (2.12)$$

Using Maxwell's equations it is possible to find a general wave equation for an electric field in matter.² In this case, the general equation simplifies to

$$\nabla^2\mathbf{E} = \frac{1}{c^2} \left(1 + \frac{Nq^2}{m\epsilon_0} \cdot \frac{1}{\omega_0^2 - \omega^2 - i\omega\gamma} \right) \ddot{\mathbf{E}} \quad (2.13)$$

Guessing a solution to equation 2.13 of the form

$$\mathbf{E} = E_0 e^{i(\mathcal{K}z - \omega t)} \quad (2.14)$$

yields a solution provided that the complex wavenumber \mathcal{K} satisfies

$$\mathcal{K}^2 \frac{c^2}{\omega^2} = \left(1 + \frac{Nq^2}{m\epsilon_0} \cdot \frac{1}{\omega_0^2 - \omega^2 - i\omega\gamma} \right) \quad (2.15)$$

The wavenumber \mathcal{K} is simply related to the complex index of refraction \mathcal{N} by

$$\mathcal{N} = \frac{c}{\omega} \mathcal{K} \quad (2.16)$$

²For a more comprehensive treatment of this subject, refer to Chapter 6 of [Fow75]

Breaking the complex index of refraction into real and imaginary parts ($\mathcal{N} = n + i\kappa$) gives a rewritten version of the solution (equation 2.14)

$$\mathbf{E} = E_0 e^{-\frac{\omega}{c}\kappa z} e^{i(\frac{\omega}{c}nz - \omega t)} \quad (2.17)$$

This shows that the complex index of refraction affects the electric field component of the laser in two ways. The real part of the index of refraction, n , affects the phase of the light ($D(\omega) \propto n$ where $D(\omega)$ is the dispersion), while the complex part, κ affects the absorption ($A(\omega) \propto \kappa$). Solving for n and κ using equation 2.15 yields

$$n = 1 + C \frac{\omega_0 - \omega}{(\omega_0 - \omega)^2 + (\gamma/2)^2} \quad (2.18)$$

$$\kappa = C \frac{\gamma}{(\omega_0 - \omega)^2 + (\gamma/2)^2} \quad (2.19)$$

where C is a constant proportional to the rate of absorption of light. γ characterizes the linewidth of the transition determined by homogeneous broadening effects (such as collision and state lifetimes), assuming no Doppler broadening. In an actual spectroscopic experiment, the homogenous effects (which are Lorentzian in shape as evidenced in equation 2.19) combine with Doppler broadening (which is Gaussian) to create a lineshape known as a Voigt profile.

In the work presented in this thesis, the phase shift caused by the real part of the index of refraction in the light/thallium interaction is measured using a differential signal technique that is highly sensitive to such shifts. Other more typical spectroscopic techniques can just measure absorption, which is the effect of κ , the imaginary component of the index of refraction. Because of the effect the phase shift has on our ring cavity optical system (see chapter 3), both effects (the phase shift due to n and the absorption due to κ) can be seen. For a simulation of the lineshapes and experimental signal for the $6P_{1/2} \rightarrow 6P_{3/2}$ transition, refer to chapter 2 of [But06].

Chapter 3

Experimental Techniques and Implementation

The experiment setup for this work is a complex combination of optics to process and deliver laser light to an interaction region containing thallium. As thallium is a metal at room temperature and this work involves studying a weak transition, it is necessary to heat the thallium to $\sim 800^\circ\text{C}$ to reach a sufficiently high vapor pressure to perform useful spectroscopy. This, combined with a need to eliminate Doppler broadening and provide an environment amenable to large electric fields, led to the development of an atomic beam apparatus where vaporized thallium and laser interact perpendicularly in a high vacuum environment. A novel three mirror Fabry-Perot ring cavity was also developed to allow counterpropagating laser beams to interact with the thallium beam and be measured using a low noise differential signal technique. The precision of the differential signal method requires active stabilization (locking). Finally, to improve the frequency control over the laser, an active stabilization system was implemented for the laser as well. Reference figure 3.4 for a graphical layout of the experimental setup explained throughout this chapter.

3.1 Differential Signal Method

The 1283 nm transition is a magnetic dipole / electric quadropole (M1/E2) transition. The electric dipole (E1) is not allowed (see section 2.1), and since the electric dipole moment is much larger in atoms than the magnetic dipole, the probability of excitations is small in this transition, thus showing weak absorption. Combined with a relative small number of atoms the laser interacts with due to the atomic beam apparatus geometry (see section 3.4), the signal expected for studying this transition is small. To detect such a signal, a sensitive, low noise technique is necessary. One possible way to accomplish this is using RF spectroscopy as described in [Sim07]. A different approach was taken in this work, however. The differential technique presented here takes two beams originating from the same laser and experiencing similar environmental conditions and subtracts them. The commonality between the

signals means that much of the noise (acoustic, mechanical, electrical and laser frequency drifts) in the system is removed. Figure 3.1 demonstrates common mode noise rejection for the ideal case (where both signals experience identical noise).

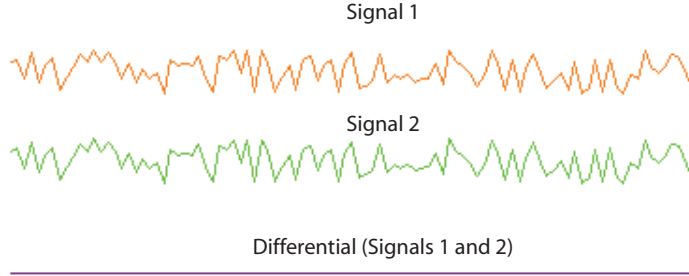


Figure 3.1: Simulation of ideal common mode noise rejection. Signals 1 and 2 originate from the same source and experience the same environment.

Clearly, if the two signals are identical in all respects, the differential method removes any experimental signal as well, which would be silly. This experimental setup uses two signals that are similar in many respects to sources of noise, but different in such a way that a spectroscopic signal can be observed. For the proposed isotope and Stark shift measurements, this involves starting with a single laser beam, splitting it, and shifting the frequency of one beam such that it is no longer resonant with the atomic transition. When one beam interacts with the atomic transition, it is phase shifted and attenuated by the real and complex parts of the index of refraction, respectively. The other beam is shifted off the transition, so it is unaffected. In this case, the difference between the signals from the two beams is nonzero.

The two signals are passed through a Fabry-Perot ring cavity which allows sensitive detection of the phase shift component of the light-atom interaction. The frequency shifted beam is shifted by precisely one free spectral range of the ring cavity (438 MHz) so that the peaks of the resulting Airy function line up (as the Airy function is periodic), and the differential signal is zero except in the presence of the atomic interaction. The basics of the differential signal method are summarized in figures 3.2 and 3.3. In figure 3.2 (a), both beams are the same frequency, and the differential signal would be zero except for effects that depend on the direction of propagation (as in the proposed TOPE experiment). In (b), one beam is frequency shifted up from the other. In short, the periodic nature of the Airy function means that the cavity does not "care" about the frequency shift, but the atoms do. This is the present configuration of the system for isotope and Stark shift measurements.

Figure 3.3 (a) shows a single set of peaks where both beams are off resonance with the atomic transition. (b) demonstrates the case where one beam is on resonance. The

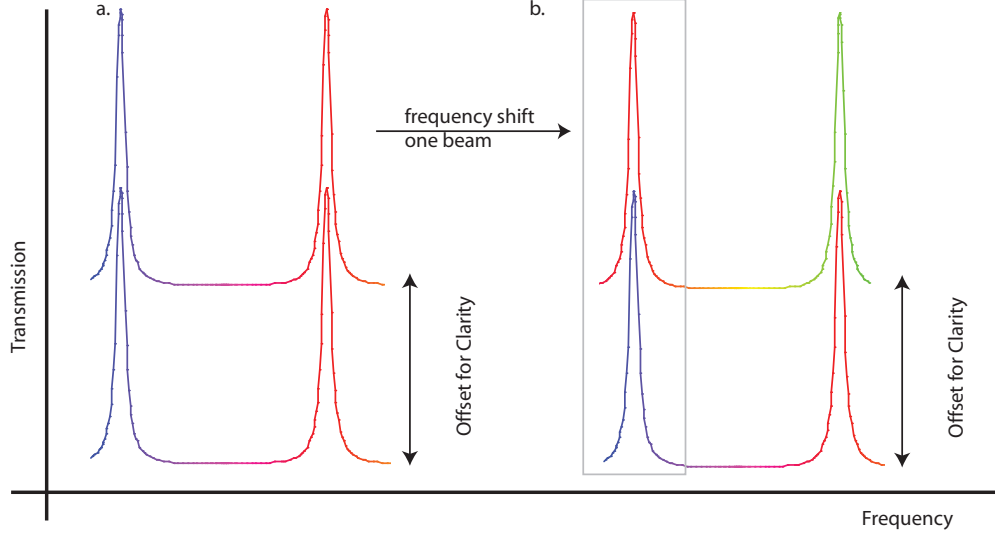


Figure 3.2: Simulation of the output of the Fabry-Perot ring cavity demonstrating the frequency shifting of one beam. In (a), both beams are the same frequency. In (b) one beam is shifted by exactly one free spectral range. The boxed portion of (b) corresponds to figure 3.3 (a).

effect of the phase shift and attenuation caused by the complex index of refraction is exaggerated. The lock point of the active stabilization circuitry is marked (the inflection point, i.e. $\sim 70\%$ of the Airy function peak). (c) is a simulation of the expected differential signal for a single atomic transition out of the four expected ($F = 1 \rightarrow F' = 1$ and $F = 1 \rightarrow F' = 2$ for both isotopes). The relative positions of the differential signal (gray), unshifted beam (purple) and shifted beam (red) are marked.

3.2 Optics

The system is configured currently for isotope and Stark shift measurements, both which require the laser frequency to be scanned across the absorption spectrum so that only one beam at a time is resonant with the atomic transition at a time. Thus, the differential signal is nonzero. The somewhat complex optical setup running from the laser to the atomic beam apparatus is designed to split the laser light into two beams, one at the original frequency from the laser and one frequency shifted up by a known amount (which is one free spectral range of the ring cavity, as explained above) and deliver it into the ring cavity. It is useful to examine figure 3.4 while following the beam path starting at the laser and working to the atomic beam apparatus:

- Single mode light at 1283 nm leaves the laser with ~ 12 milliwatts of power. See appendix section A.1 for details on the laser.

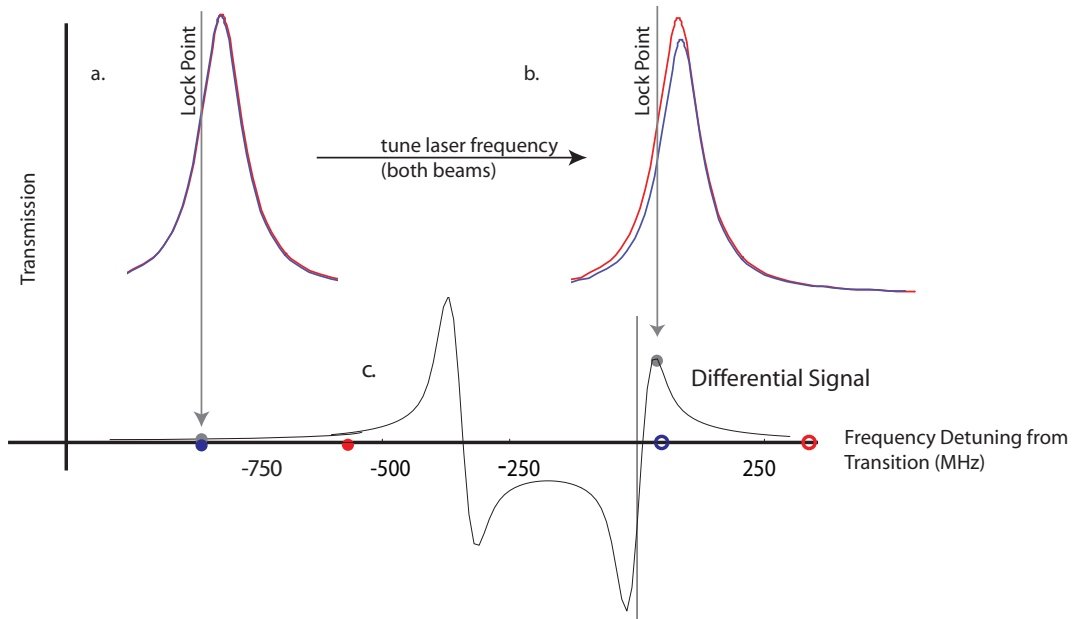


Figure 3.3: Simulation of the differential signal. (a) shows the output of the ring cavity when both beams are off resonance with the atomic transition. The differential signal (c) is measured from the lock point shown. (b) illustrates the two signals when one is on resonance. The expected differential signal for a single peak is shown in (c), which is adapted from models done by Butts in [But06]. A single beam interacting with the atomic transition leads to a differential signal that is the derivative of a dispersion curve. As both beams interact with the atomic transition during the scan, two of these dispersion derivative lineshapes are present.

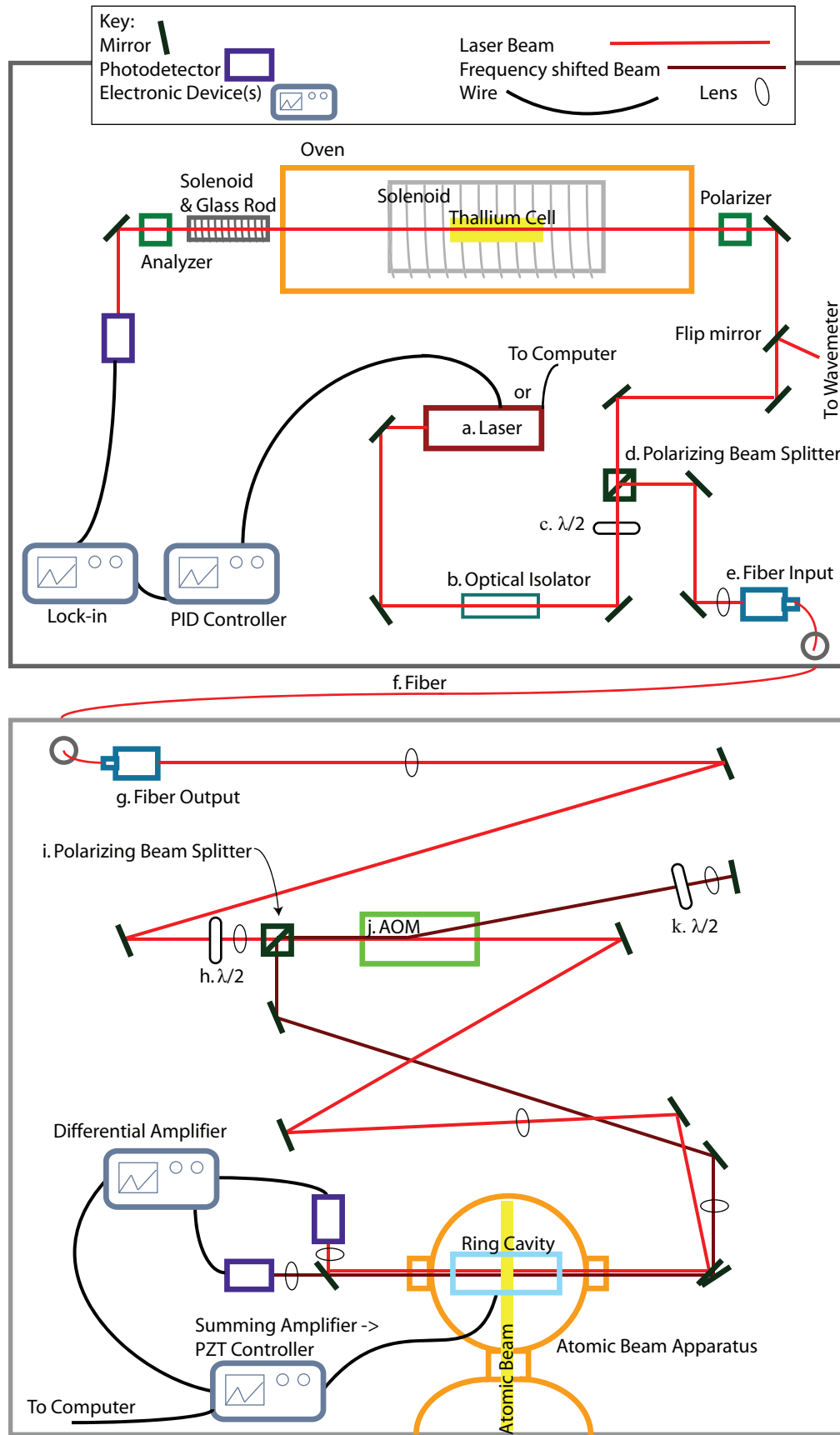


Figure 3.4: Schematic of Experimental Apparatus including the general layout. Some details have been omitted or modified for clarity.

- The light passes through an optical isolator so that back reflections anywhere in the optical system do not disrupt the laser. This is a common problem with diode lasers.
- A half wave plate and polarizing beam splitter splits the light between the laser locking system (discussed below in section 3.7), which occupies much of the remainder of this optical table, and the atomic beam system. The light is currently split in a ratio of power of 1 to 6, where the atomic beam system receives the majority of the light.
- A single mode optical fiber is used to transport the light from the originating table to the second optics table where the atomic beam apparatus resides. About 75% of the light power is lost aligning the beam into the fiber input, but the loss is worth the high quality and stable beam that comes out of the fiber. The output coupler is comprised of a mount that holds a chuck with the fiber exposed at the end and a small collimating lens. The chuck can move in three dimensions. The alignment of the fiber and the lens is critical; if the fiber is not precisely centered on the lens, miniscule natural drifts (over a few days) leads to large changes in the alignment of the beam coming out of the entire output coupler as the edge of a lens tends to steer the beam.
- The light is steered and focused into an acousto-optic modulator (AOM) that takes output from a synthesizer and produces a sound wave which frequency shifts (and deflects) a portion of the laser light (roughly 20%). The shifted light is passed back through the AOM to yield a beam that is frequency shifted at twice the synthesizer input. The total shift is currently set at 438 MHz, the free spectral range of the Fabry-Perot ring cavity. A half wave plate aligns the light with the transmission axis of a polarizing beamsplitter. This polarizing beamsplitter is used to pass essentially all the incoming light, but it reflects all the double passed frequency shifted light. The frequency shifted beam is reflected as it has been rotated by 90° by two passes through another half wave plate.
- Both beams are now steered into the atomic beam apparatus in such a way that the frequency shifted beam circles the cavity in the counterclockwise (CCW) direction (facing the atomic beam apparatus from the location of the fiber) and the unshifted beam circles clockwise (CW).

The Fabry-Perot ring cavity produces output in the form of an Airy function as a function of frequency. The Airy function peaks of the two beams overlap, since the frequency shifted beam is precisely one free spectral range offset from the unshifted beam. The two beams are steered into two photodetectors (with built-in preamplifiers) and subtracted using an external differential amplifier. The signals can be analyzed and recorded at this point, and the unshifted beam is used to lock the cavity. For the future TOPE experiments, the frequency shift between the beams would

not be desired, and the AOM and associated optics could be replaced with a simple beamsplitter. For further details on the experimental configuration required for the TOPE experiment, see section 6.5.

3.3 Fabry-Perot Ring Cavity

The ring cavity (pictured in figure 3.5) is functionally similar to a standard two mirror Fabry-Perot cavity with the addition of a third mirror. The three mirror configuration allows two beams to propagate in opposite directions but interact with the same atomic beam (see figure 3.6). Counterpropagating beams are necessary to test for time reversal symmetry violation, which is the eventual goal of this work. The ring cavity can be tuned with a three axis ThorLabs piezo electric transducer stack. Presently, all three axes are electrically connected and controlled by one voltage source to change the length of the cavity. Tuning the axes separately could be done to better align beams within the cavity, if desired.

3.4 Atomic Beam Apparatus

The Fabry-Perot ring cavity is housed within the atomic beam apparatus, a system designed to deliver a narrow beam of atoms perpendicular to the laser beams. Thallium is heated in an oven in one chamber of the apparatus to $\sim 800^\circ\text{C}$. It escapes through a slit and travels through to the second chamber (the interaction region) where the ring cavity is housed. Between the cavities is a set of four adjustable collimating slits. Finally, the beam travels through a plexiglass shield that also has a slit. The three sets of slits ensures that the atoms that interact with the atoms are truly traveling in a straight line. This geometry eliminates Doppler broadening from the atomic spectrum as all the atoms have no component of velocity in the direction of the laser beam.

In the present work, the ring cavity has been protected from possible thallium contamination on the mirrors by a front plate with a slit to allow the atomic beam to pass (figure 3.6) and a three sided shield (which has narrow holes for the laser beam). A helium neon laser was used to ensure the atomic beam collimating slits are at the proper height so that the atomic beam intersects with the laser beam.

The atomic beam apparatus is evacuated by a system of vacuum pumps which achieves 10^{-7} torr at room temperature and 10^{-5} when the oven is running. Too much background gas in the cavity would disrupt the atomic beam and potentially contaminate the hot thallium source.

3.5 Cavity Locking

In order to be maximally sensitive to phase shifts, the ring cavity must be held near the inflection point on the side of a peak in the Airy function. This way, a small

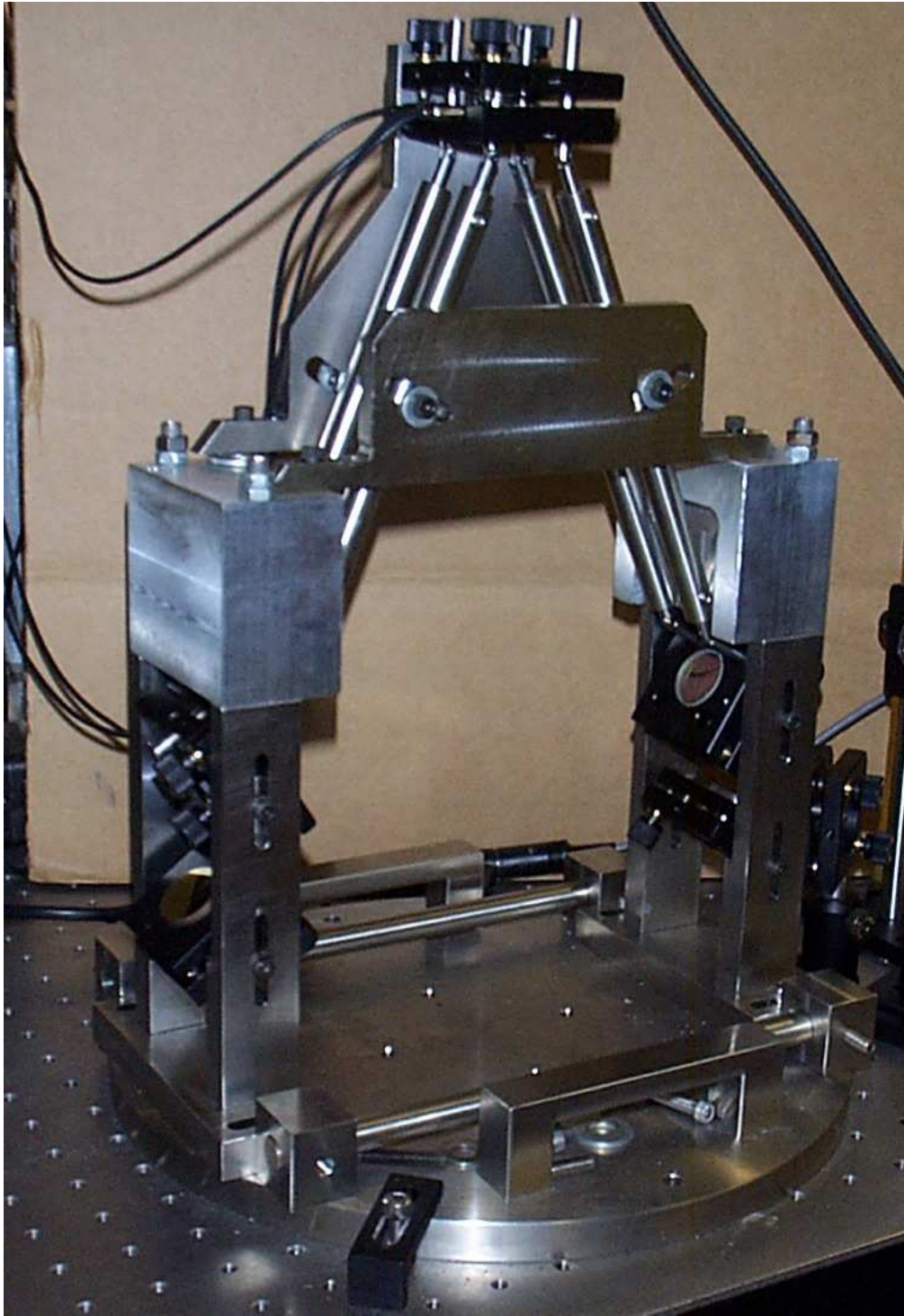


Figure 3.5: Photograph of the Fabry-Perot ring cavity.

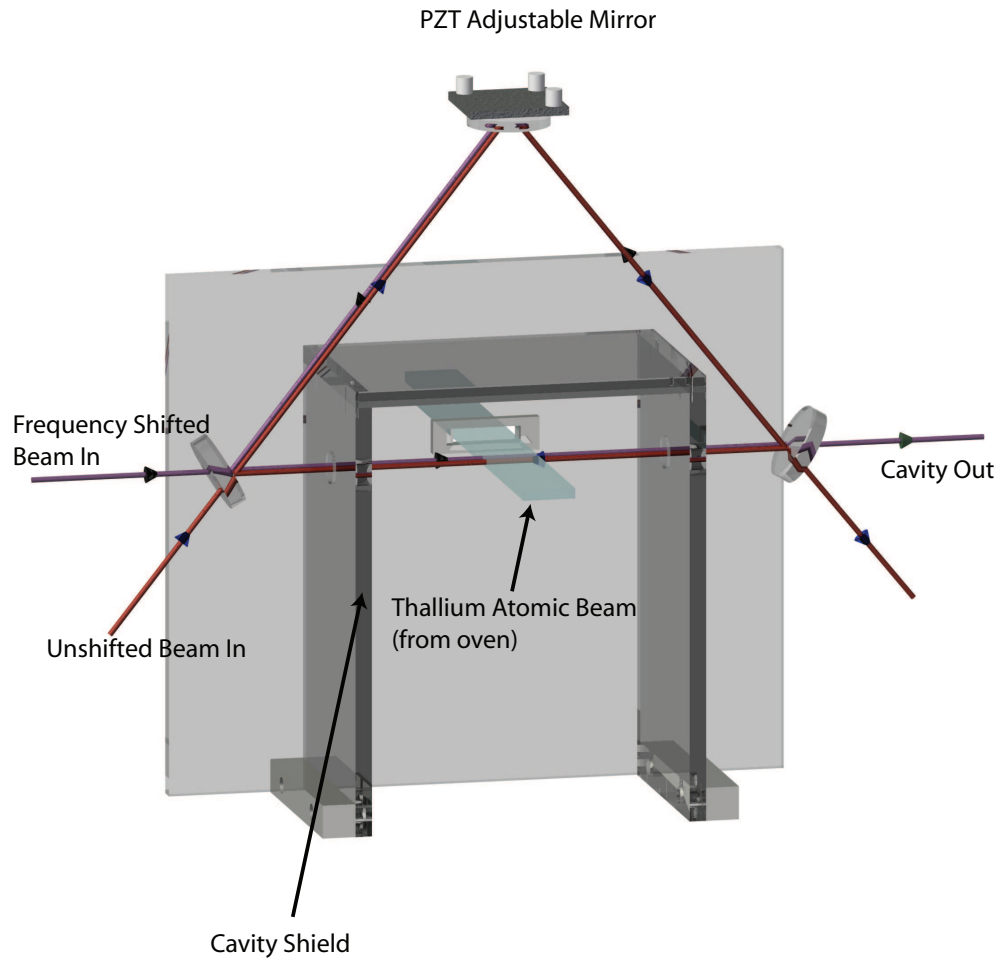


Figure 3.6: Rendered model of the Fabry-Perot ring cavity with counterpropagating laser beams interacting perpendicularly with the atomic beam. The actual ring cavity structure is not shown, only the mirrors. Note the cavity shield which was added to protect the mirrors from stray thallium.

optical path length change in one beam relative to the other will cause a large change in the differential signal as seen in (a) and (b) of figure 3.3. Drifts in the laser frequency, as well as thermal and mechanical drift in the cavity itself, causes the optical transmission signal of the cavity to move away from the ideal set point.

To keep the output to the desired inflection point, an active locking system is employed. The signal from the stronger unshifted beam is sent to a PID controller that is set to lock in the steepest part of the peak (~ 0.7 times the peak height). The PID controller sends a correction signal, proportional to the difference between the setpoint and the present value, that is fed to a piezo electric transducer stack mounted on the top mirror of the ring cavity. In this way, the length of the cavity is actively steered to compensate for the above-mentioned drifts.

3.6 Summing Amplifier

As discussed in section 3.1, the differential signal method used to reject common mode noise and thus resolve the experimental signal requires locking the ring cavity to the side of a Fabry-Perot peak on one of the beams (in the current experimental setup, the lock is performed on the beam that is not frequency shifted, i.e. the stronger beam). The Stanford Research Systems (SIS) proportional-integral-derivative (PID) controller (Model SIM960) used to lock the ring cavity produces a correction signal that can range from -10 to 10V. However, this PID controller also has a minimum setting for the proportional gain of 0.1 times the deviation of the input signal (in our case the amplitude of the unshifted beam) to the setpoint (~ 0.7 times the Fabry-Perot peak maximum). Even this minimum correction is still too large for the ring cavity system; it is driven into severe oscillations around the lock point.

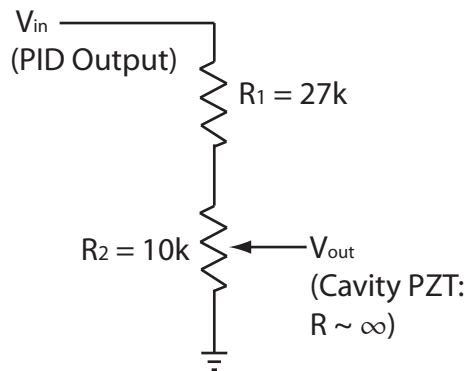


Figure 3.7: Voltage Divider to attenuate PID output to prevent overdriving off the lock system.

The solution to this problem was simply to attenuate the correction signal of the PID controller before feeding it into the cavity PZT controller, which has a built in ten times amplifier. This was initially done with a two resistor variable voltage

divider as shown in figure 3.7. Since the PZT has a very large impedance, the signal sent to the PZT controller from the divider was adjustable from 0.27 to 0 times the PID correction signal as $R_1 = 27k\Omega$ and $R_2 = 0 \rightarrow 10k\Omega$. The actual amount of attenuation provided by the voltage divider was tuned using the potentiometer to provide a tight lock without overdriving and was experimentally determined to be ~ 0.1 .

$$V_{out} = \frac{V_{in}R_2}{R_1 + R_2} \quad (3.1)$$

However, while this simple solution allowed for stable locking of the cavity system, it was not satisfactory for scanning the laser over ranges of more than a few hundred megahertz, which is not sufficient for scanning over the ~ 2 GHz atomic resonance spectrum of interest. Changing the wavelength of the laser requires changing the optical path length of the cavity to maintain the same position on the Fabry Perot peak where the system is locking. Specifically, decreasing the voltage to the laser PZT leads to a lowering of the frequency of the laser. This corresponds to a longer wavelength, and thus the cavity must be lengthened. This is done by shortening the length of the cavity PZT, which is effected electrically by decreasing the voltage to this PZT. The PID controller can make this adjustment to the error signal as the frequency changes (assuming it is sufficiently slow to allow for correction), but it is limited by a -10 to 10 volt output range. Since the signal is attenuated by roughly a factor of ~ 10 by the voltage divider before entering the cavity PZT controller (which then multiplies it by 10), the effective usable range on the PZT is about 20 volts out of a possible 150 volts. This can only compensate for a few hundred megahertz of laser tuning range. While sufficient for the corrections the cavity lock must make for mechanical and thermal noise in the system, it was not effective for laser scans of multiple gigahertz.

The solution to this problem was to add a portion of the scan signal sent from the computer to the laser to the PID correction signal and then send that resulting signal to the cavity PZT controller. Thus, since the gross correction needed to the cavity length is directly proportional (at least to a good first order approximation) to the change made to the laser frequency, this is an effective correction. This task was accomplished by using a summing amplifier composed of a single operational amplifier (op amp). Two more op amps were used before the summing amplifier to adjust the gain of the input signals (PID correction signal and computer scan signal). The inverting amplifier gain is simply $-R_2/R_1$ where R_1 is the input resistor and R_2 is the feedback resistor. The equation for the final amplifier is the inverted weighted sum of the two inverting preamps (schematic and resistor values are given in figure 3.8)

$$V_{out} = -\left(\frac{-V_{computer}R_1(R_5 + POT_1)}{R_3R_7} + \frac{-V_{PID}R_1(R_4 + POT_2)}{R_2R_6}\right) \quad (3.2)$$

Since the summing amplifier has the same value resistors (R_1 through R_3) for the

inputs and the feedback its gain is 1. Thus, equation 3.2 simplifies to

$$V_{out} = -\left(\frac{-V_{computer}(R_5 + POT_1)}{R_7} + \frac{-V_{PID}(R_4 + POT_2)}{R_6}\right) \quad (3.3)$$

Designs for the three amplifiers were based on material contained in [HH89]. The final circuit, constructed using a hybrid of soldering and wire wrapping techniques, is photographed in figure A.3. The values for the amount of amplification (or attenuation in the case of the PID correction signal input) were experimentally determined and then values of resistors were picked to minimize the load on the inputs. The op amp used is a LF347 quad op amp and the circuit is powered by a New Focus ± 15 volt, 0.1 ampere power supply.

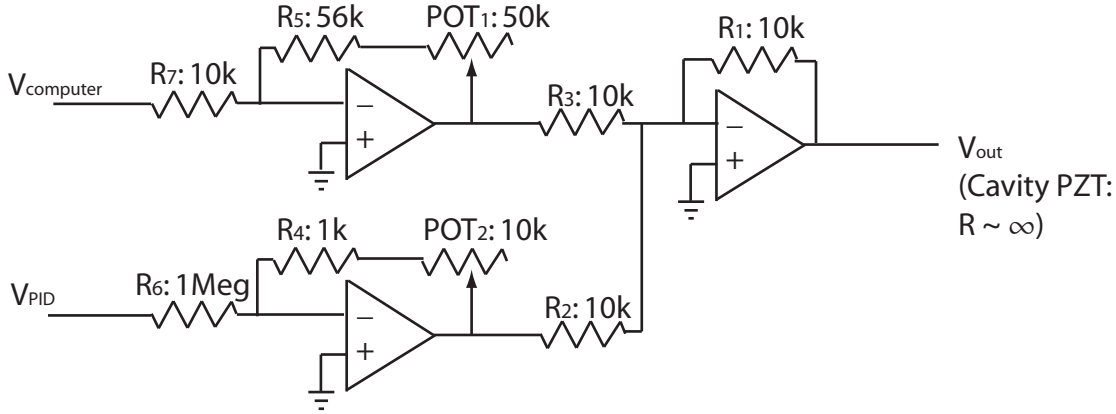


Figure 3.8: Electrical Schematic of a Summing Amplifier for the Cavity Lock System. Note that both preamplifiers are inverting as is the summing amplifier, thus yielding an output that is directly proportional to the sum of both inputs (not negative) as desired.

The end result is a robust cavity locking system that can be scanned over multiple gigahertz and remain consistently locked. The entire cavity locking system, with corresponding voltage ranges on all connections is diagrammed in figure A.4. Reference chapter 4 for details on performance.

3.7 Exploiting Faraday Rotation for Laser Stabilization

Returning to the laser's optical table in figure 3.4, the light split by the polarizing beamsplitter (d) and not sent to the fiber is used for two purposes. It can be sent by a flip mirror to a Burleigh WA1500 wavemeter. This allows a coarse measurement of the laser's frequency, which is helpful for tuning the laser near the transition. With the flip mirror down, however, the light travels through a polarimeter containing a

thallium vapor cell. The output of the polarimeter is an atomic lineshape which has a steep linear region. By using a PID controller to lock to this feature, the frequency of the laser can be tightly controlled.

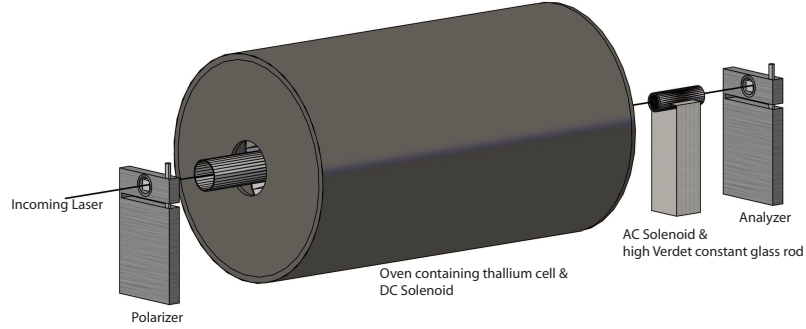


Figure 3.9: Diagram of the polarimeter setup for the laser locking system.

The diode laser used for these experiments (detailed in A.1) is subject to long and short term drifts in frequency due to thermal and mechanical fluctuations in the diode and grating. A method of locking the laser by exploiting Faraday rotation is detailed initially in [KBUM05] and [Ker05] and further in [But06]:

- About 2 mW of the laser is taken off using a polarizing beam splitter and sent into the laser locking apparatus.
- This light is linearly polarized by a high quality calcite prism polarizer.
- It is then passed through a thallium vapor cell (and supporting oven to reach 800°C at which temperature the vapor pressure is sufficient for measurable absorption). The cell itself is within an evacuated tube to reduce the noise caused by the convection of hot air. The vapor cell is inside a DC solenoid that provides a 10 G magnetic field parallel to the light which in turn causes a Zeeman splitting of the energy levels. The Zeeman splitting causes a difference between the absorptions of the two circular components (left and right) in the incident laser light. As linearly polarized light can be thought of as a mixture of left and right circularly polarized light, the resulting rotation ($\Phi_F(\nu)$) in the linearly polarized light is equivalent to the derivative of the dispersion curve of the resonant transitions [KBUM05].
- Following the vapor cell, the light is passed through a high Verdet constant glass rod. The glass rod is surrounded by a solenoid driven by AC current at ~ 700 hertz (ω_m). This induces a sinusoidal time varying polarization of the light.
- A second calcite prism polarizer serves as the analyzer for the polarimeter. The entire polarimeter setup is diagrammed in figure 3.9. The resulting intensity of

the signal is the sine squared of the sum of the induced rotations (atomic cell and glass rod) (equation 3.4).

$$I(t) = I(\nu) \sin^2(\Phi_m \sin(\omega_m t) + \Phi_F(\nu)) \quad (3.4)$$

These rotations are small, and thus the first order approximation $\sin^2(\Theta) \approx \Theta^2$ is excellent. By applying this approximation and expanding (equation 3.5), the resulting intensity clearly has a component at ω_m that depends on $\Phi_F(\nu)$ and Φ_m , both to first power, which is much larger than the squared components.

$$I(t) \approx I(\nu) [1/2 \Phi_m^2 + \Phi_F^2(\nu) - 1/2 \Phi_m^2 \cos(2\omega_m t) + 2\Phi_m \Phi_F(\nu) \sin(\omega_m t)] \quad (3.5)$$

Passing the resulting light through a lock-in at ω_m picks off this desired component. The final signal, $\Phi_F(\nu)$, is manifest as a derivative of the dispersion curve of the Doppler broadened 1283 nm transition. The region around the zero optical rotation point has a steep linear slope. The signal is then input to a PID controller (SRS SIM960) which corrects for drifts away from the zero crossing by varying the voltage applied to the laser PZT (see section A.1). The result is a laser with frequency stability of ≤ 1 MHz. However, this is only useful when the laser is not being scanned, or if the scanning is very slow. See chapter 3 of [Ker05] for more details about this laser stabilization system.

The laser locking system was also the subject of recent technical work, which is outlined in appendix B.

Chapter 4

System Performance

4.1 Stability of Optics

Before delving into the quantitative details of the performance of the experimental system, it is useful to note several long time scale observations about the system. The optics stay in reasonable alignment for weeks, only requiring minor adjustments to the mirrors and other optical devices to maximize transmission through the Fabry-Perot ring cavity. The alignment for the optics before the fiber can be done separately from the alignment after the fiber, allowing for relative ease in maximizing the signal before running tests. While complete alignment starting with no output from the ring cavity can take many hours, the time needed to tweak the system to its highest throughput on a daily basis is substantially less than one hour. The realignment of the output fiber coupler discussed in chapter 3 and the replacement of several lenses has greatly contributed to this long time scale stability.

4.2 Laser Scanning

Since the frequency tuning of the laser is accomplished by moving a diffraction grating (see appendix section A.1), it is reasonable to suppose that tuning the frequency of the laser would cause beam steering. This combined with a difference in lasing quality over different frequencies leads to a varying intensity of the laser that reaches the output of the fiber, (g) in figure 3.4. An example scan of the laser intensity as a function of frequency is present in figure 4.1. This varying intensity would have to be accounted for, along with the differential background scan presented in figure 4.5, in measurements where the amplitude of the experimental signal was crucial. For frequency spacing measurements, such as the isotope shift experiment, the precise amplitude is not important. The frequency is highly important, thus the need for a technique for calibrating the frequency of a laser scan as discussed in chapter 5.

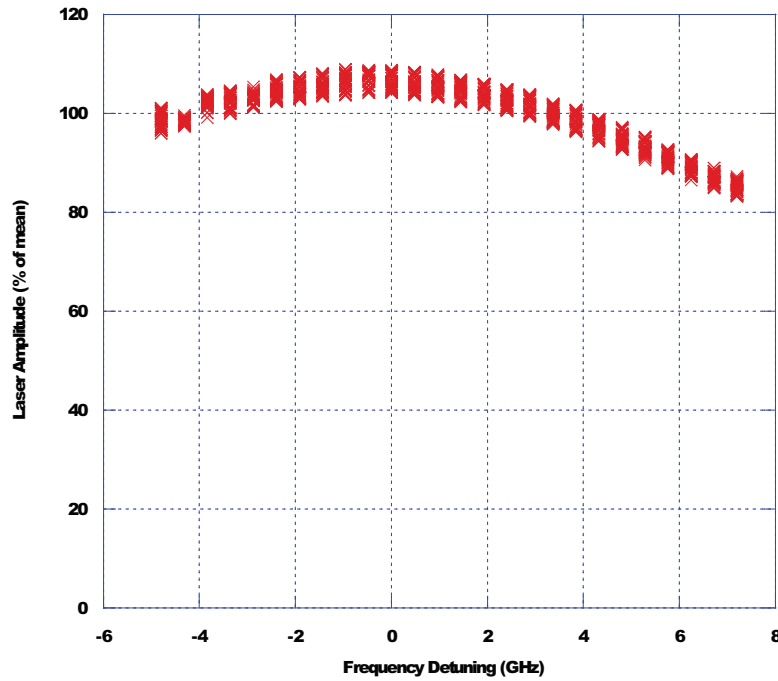


Figure 4.1: Laser output after fiber output coupler as a function of frequency.

4.3 Differential Signal

The success of the differential signal to reject noise is crucial to the ability to see the weak experimental signals we expect. Since both beams originate from the same laser and follow a similar path after being split, much of the noise present in one beam should be present in the other. By subtracting the two beams, much of this common mode noise is rejected.

It is necessary to align the two signals precisely to minimize the noise in the differential signal. The technique developed so far is:

1. Use a function generator to scan the ring cavity through a number of modes.
2. Maximize the power on the frequency shifted beam by adjusting the optics, shown by (a) in figure 4.2. Match the amplitude of the unshifted beam to that of the frequency shifted beam by attenuating the former.
3. Zoom to a single Fabry-Perot peak on each beam and signal average to better see the location and shape of both peaks, shown by (b) in figure 4.2.
4. Match both peak shapes by adjusting the amplitude of the unshifted beam and by adjusting the frequency of the AOM synthesizer (which adjusts the frequency shift of the CCW beam).

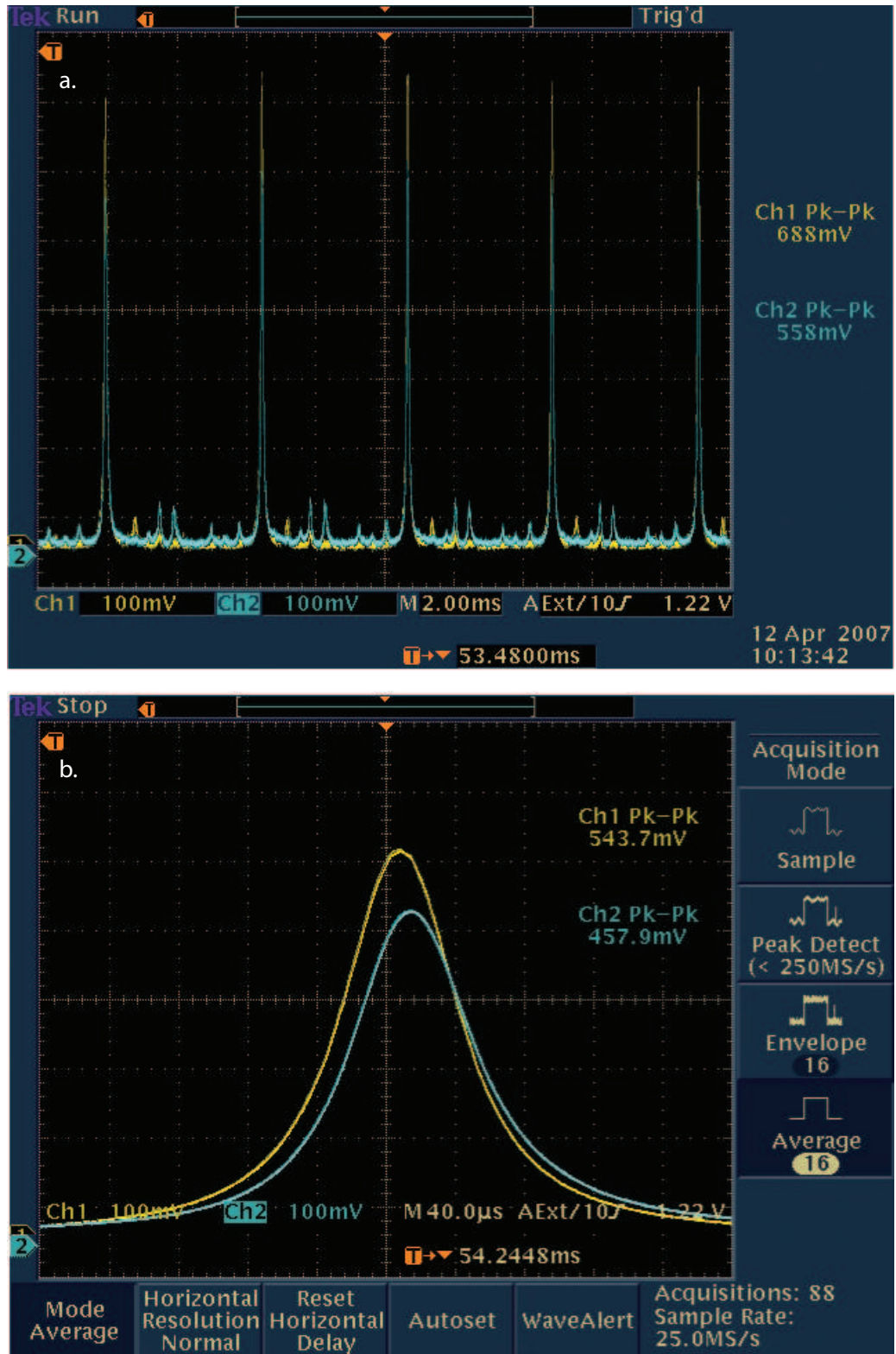


Figure 4.2: Demonstration of minimizing noise on the differential signal by aligning CW (unshifted, yellow) and CCW (frequency shifted, blue) output signals. (a) demonstrates maximizing power on both beams. (b) demonstrates signal averaging both beams. Not shown is the final step of aligning both beams to match in amplitude and frequency. The undesired "miniature" peaks visible in (a) are due to imperfect mode matching within the ring cavity, and are reduced by good alignment.

5. Stop scanning the cavity and lock to the side of the peak. Slightly adjust the amplitude and frequency again to minimize the RMS noise on the differential signal.

The next series of performance measurements on the differential signal are done with the cavity locked by the mechanism described in section 3.5 and the atomic beam not present.

4.3.1 Noise with Laser Unlocked

The noise reduction typically seen in the case where the laser is unlocked is ten times. Figure 4.3 shows the two counterpropagating signals from the ring cavity along with the difference of the two. In this figure, the cavity is being actively locked, but the laser is left unlocked. The RMS noise of the differential signal (7.12 mV) is $\sim 1\%$ of the peak height of the Fabry-Perot peak. The bandwidth (defined as the corner frequency of a low pass filter $f_{corner} = 1/(2\pi\tau)$) of the differential amplifier was 3.0 kHz. This is the most restrictive filter in the system; thus, assuming the noise is white (equal power at all frequencies), properly averaging for one second would give a noise value of $0.13 \text{ mV}/\sqrt{\text{Hz}}$ (i.e. $7.12 \text{ mV}/\sqrt{3000\text{Hz}}$) or $\sim 0.2\%$ of the Fabry-Perot peak.

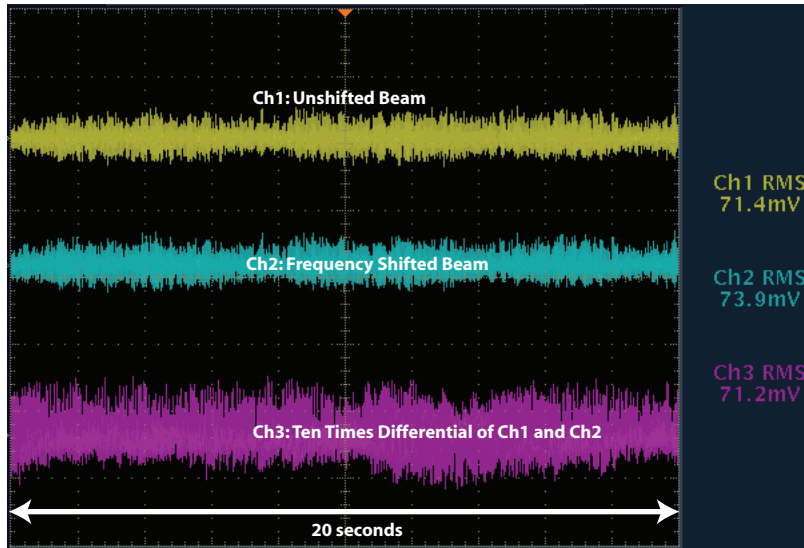


Figure 4.3: Oscilloscope trace demonstrating the common mode noise rejection of the differential signal with the *laser unlocked but not scanning*. Note that the root-mean-square (RMS) of the signals are all similar, and the differential signal is shown ten times amplified. The Airy peak height for both shifted and unshifted beams is 550 mV. The ring cavity is locked using a PID controller time constant of 1 ms, and the differential signal amplifier was set to a bandwidth of 3 kHz.

4.3.2 Noise with Scanning Laser

To take the isotope and Stark shift measurements, it is necessary to scan the laser over the atomic transition. New hardware was developed to allow scanning the laser frequency while maintaining cavity lock (see appendix A). The overall noise on the experimental signals increases when scanning the laser (figure 4.4) over the free running (figure 4.3) laser; however, the differential signal is not substantially noisier ($0.16 \text{ mV}/\sqrt{\text{Hz}}$ for scanning versus $0.12 \text{ mV}/\sqrt{\text{Hz}}$ for the representative samples presented here).

It is possible to scan the laser fast enough (greater than 5 Hz) to employ realtime signal averaging from one scan to the next on the digital oscilloscope. This may prove useful to preliminary searches for the atomic signal. Reference section 3.6 for details on the apparatus that makes this scanning possible and section 6.2 for the technique.

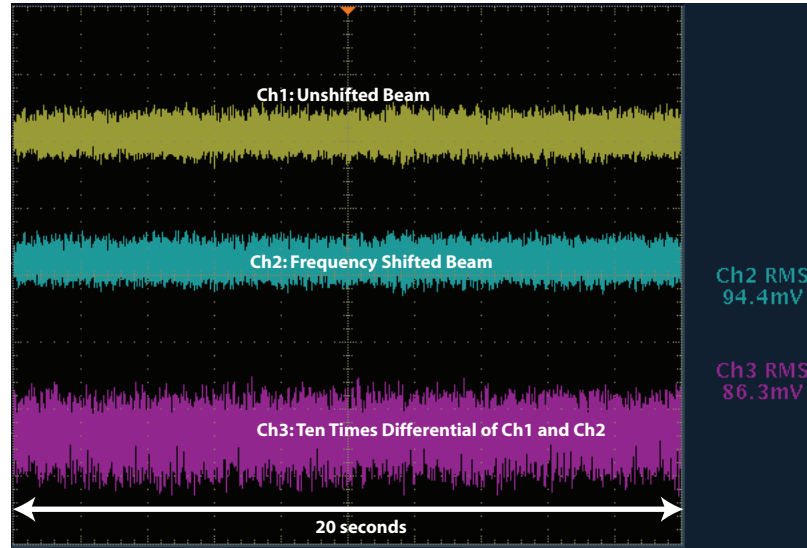


Figure 4.4: Oscilloscope trace demonstrating the common mode noise rejection of the differential signal with the *laser scanning at 5 Hz* over 1 GHz around the 1283 nm (233612.7 GHz) transition. As in figure 4.3 the root-mean-square (RMS) of the signals are all similar, and the differential signal is shown ten times amplified. The Airy peak height for both shifted and unshifted beams is 550 mV. The ring cavity is locked with a PID time constant of 10 μs .

4.3.3 Differential Signal over Long Scans

Also of interest is the behavior of the differential signal over long scans ($\sim 5 \text{ GHz}$, e.g. wider than the transition of $\sim 2 \text{ GHz}$). In the ideal situation, the differential signal should be flat throughout the entire frequency range. However, due to beam steering, the two Fabry-Perot signals do not change equally over the frequency range, and a

changing differential signal is observed (see figure 4.5.) This background will need to be measured and subtracted from any scans where this precision is necessary. As the background varies based on the exact alignment of the optics, it will probably make sense to interleave background scans with atomic scans so that the background data is accurate.

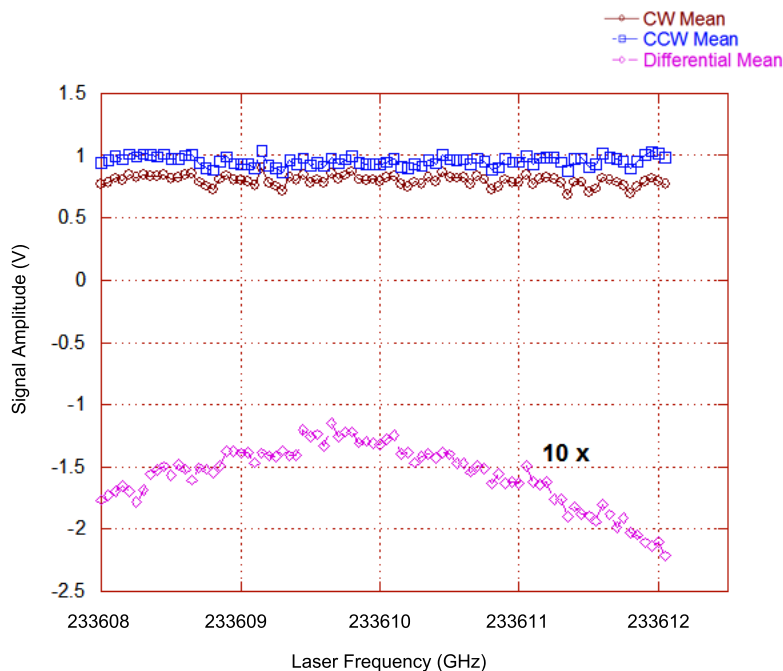


Figure 4.5: Long range (>4 GHz) scan in the region of the 1283 nm transition. The CW (clockwise) beam is not frequency shifted, while the CCW (counterclockwise) beam is. Note that the drift over this region is about 14 times larger than the short term RMS noise (as seen in figure 4.3).

4.4 Quality of Laser Lock System

While substantial data about the quality of the laser lock system has been presented in [Ker05], the system has undergone numerous improvements and repairs as explained above. Thus, several of these measurements were repeated to ensure that the quality was equal or better at present than reported originally.

The quality of the polarimeter was measured in two ways. The first was a measurement of the finite extinction, or amount of light that gets through, for crossed polarizers. The finite extinction can be modeled as a small uncrossing angle of ideal polarizers. If I_0 is defined as the initially intensity of light entering the polarimeter, the intensity output is $I_0 \sin^2(\Phi)$ for ideal polarizers. For small angles, $\sin(\Theta) \approx \Theta$. Using this approximation, it is possible to model the finite extinction of real polarizers by a small uncrossing of ideal polarizers

$$I = I_0 \Phi_0^2 \tag{4.1}$$

For the calcite prism polarizers in our setup, the finite extinction is of order $\Phi_0^2 \approx 10^{-7}$, where for ideal polarizers, Φ_0^2 would be 0. The glass surfaces of the vacuum tube, thallium cell, and Faraday rod all tend to degrade the polarization, however, leading to a higher finite extinction for the entire polarimeter. Kerckoff quotes a value of $\Phi_0^2 \approx 10^{-5}$ in [Ker05]. To measure this value, the intensity of the light was observed for completely crossed polarizers. Then, one of the polarizers was uncrossed manually a known amount using the micrometer attached to the prism mount until the intensity doubled. The angle uncrossed is then equal to the value of the "angle" of the finite extinction. For the present setup, after all the work in the polarimeter, the finite extinction was found to be on the order of 10^{-6} , a factor of ten better than previously. The improvement is likely from better alignment and cleaning of the glass surfaces in the polarimeter.

The second measurement was of the angle noise of the polarimeter, the RMS noise in the signal after passing it through the lock-in. The angle noise was found to be ~ 5 microradians, which is as good as before the repairs.

Chapter 5

Calibrating Laser Scans

As discussed in appendix section A.1, the diode laser used in these experiments is frequency controlled by moving a diffraction grating using a piezo electric transducer (PZT) stack. PZTs are inherently nonlinear in their mechanical response as a function of voltage and exhibit hysteresis. Furthermore, the laser's frequency response as a function of the grating's position is also presumed to be nonlinear. The combination of these factors means it is not possible to simply adjust the voltage applied to the laser PZT and expect the laser frequency to change by a linearly proportional amount. Since the atomic scans in this work require that the laser frequency be known precisely throughout the scan, a calibration scheme was proposed and tested. The approach is outlined in this chapter, while more technical details about the software and data processing can be found in appendix C.

5.1 Airy Functions

A fixed length Fabry-Perot cavity produces output only when the frequency of the light is such that an integer number of wavelengths fits within the cavity, allowing constructive interference between subsequent reflections of the light. The resulting curve of transmission versus frequency for such a cavity is thus a series of evenly spaced peaks, mathematically represented as an Airy function, $A(\nu)$ ¹

$$A(\nu) = \frac{A_0}{1 + \left(\frac{2F}{\pi}\right)^2 \sin^2\left(\frac{\pi\nu}{\Delta\nu}\right)} \quad (5.1)$$

where $\Delta\nu$ is the free spectral range ($\Delta\nu = \frac{c}{2L}$; L is the cavity length), F is the finesse of the cavity ($\Delta\nu/FWHM$), and A_0 is the maximum amplitude. Figure 5.1 shows the Airy functions expected for three Fabry-Perot cavities of the same length but different mirror reflectivity (and thus finesse).

¹For more details on Fabry-Perot interferometers and Airy functions, see chapter 4 of [Fow75].

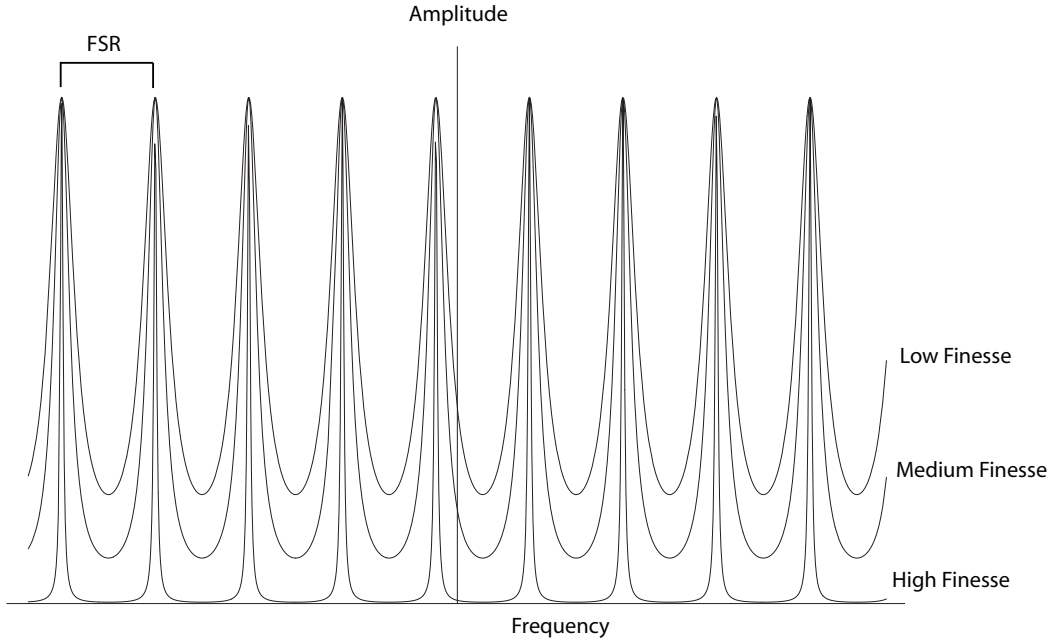


Figure 5.1: Airy functions of differing finesse.

5.2 Exploiting the Airy Function for Calibration

This calibration method uses the fact that the free spectral range is constant and known (from the dimensions of the Fabry-Perot cavity) to determine the nonlinearity of the PZT and thus correct for it in the atomic scan. The proof of concept work detailed here was done using the Fabry-Perot ring cavity without any atoms in the atomic beam apparatus. The technique could easily be used in an external two mirror standard Fabry-Perot cavity by diverting a small fraction of the laser light from the rest of the experimental setup. This will be necessary for actual atomic scans, as the ring cavity will be operated locked with atoms present. Recording data from the external Fabry-Perot simultaneously with atomic data allows for accurate calibration for each scan, so that variations in the performance of the PZT and laser from day to day, or even scan to scan, do not affect the calibration's accuracy.

The goal is to find a function for ν in terms of the voltage applied to the PZT. First, the discrete voltages (V_j) are converted to a dimensionless variable x with a range of $-1 < x < 1$ (equation 5.2).

$$x_j = \frac{2V_j - (V_{max} - V_{min})}{V_{max} - V_{min}} \quad (5.2)$$

Therefore, as ν is a nonlinear function with unknown coefficients,

$$\nu = a_0 + a_1x + a_2x^2 + a_3x^3 \dots \quad (5.3)$$

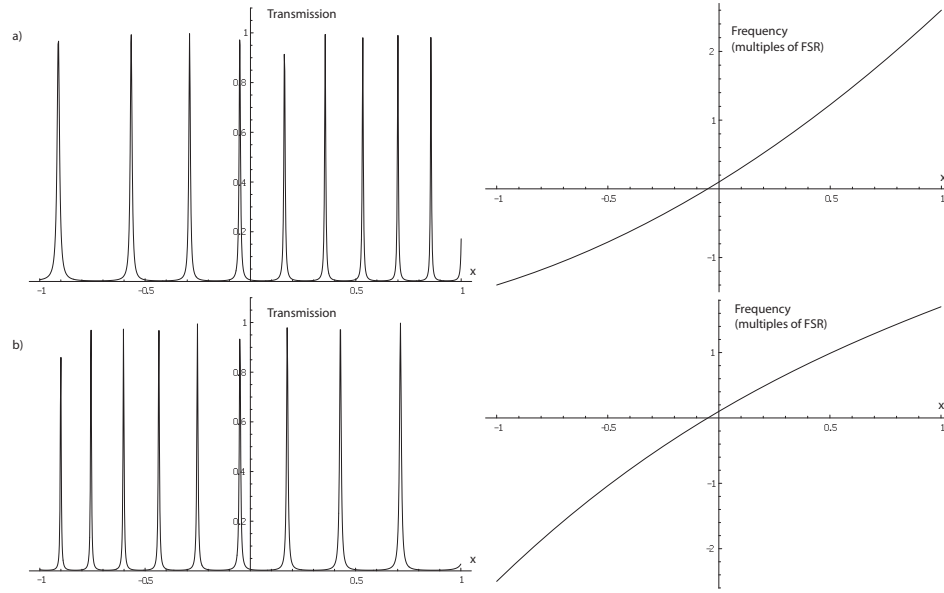


Figure 5.2: Two simulations of Airy functions (left) a function of voltage (scaled as x) showing different forms of nonlinearity. (a) has a positive quadratic term and (b) has a negative quadratic and a small positive cubic term. The right is the corresponding graph of $\nu(x)$.

Since by the way x is defined in equation 5.2, $-1 < x^n < 1$, the significance of the coefficients a_0, a_1, a_2 , etc. can be directly seen by their relative sizes. That is, without rescaling the independent variable, the n th power term could be significant, even if the coefficient was quite small due to the potentially large size of V^n . By rescaling, it is easy to quickly see which terms are significant by direct comparison of the coefficients.

Using 5.3 in 5.1 and allowing for nonlinear amplitude changes (coefficients b_0, b_1, b_2 to replace A_0) produces

$$A(\nu) = \frac{b_0 + b_1x + b_2x^2}{1 + \left(\frac{2F}{\pi}\right)^2 \sin^2 \left(\frac{\pi(a_0 + a_1x + a_2x^2 + a_3x^3 \dots)}{\Delta\nu} \right)} \quad (5.4)$$

where $\Delta\nu$ is the free spectral range (FSR) of the cavity.

The experimental data from the Fabry-Perot cavity is fit using MATLAB to equation 5.4 to obtain values for a_0, a_1, a_2 and so on up to the desired quadratic term. Coefficients b_0, b_1, b_2 , and F are not used in the calibration, but they are included to ensure a good fit. Reference appendix C for technical details on the MATLAB fitting routine. Figure 5.2 shows simulations of expected Airy functions and corresponding calibration curves (ν versus x). The nonlinearity is exaggerated from the observed effect on these simulations.

Once the coefficients are determined, the atomic scan data can be plotted on an accurate frequency axis so that the frequency difference between atomic resonance

features can be measured. Figure 5.3 shows frequency as a function of the scaled independent variable x for four scans over ~ 5 GHz. The nonlinearity is not large, but it is clearly manifest. All of these scans were taken on the same day, stressing that the nonlinearity can vary from scan to scan, thus encouraging the use of a calibrating scan simultaneously with each atomic scan.

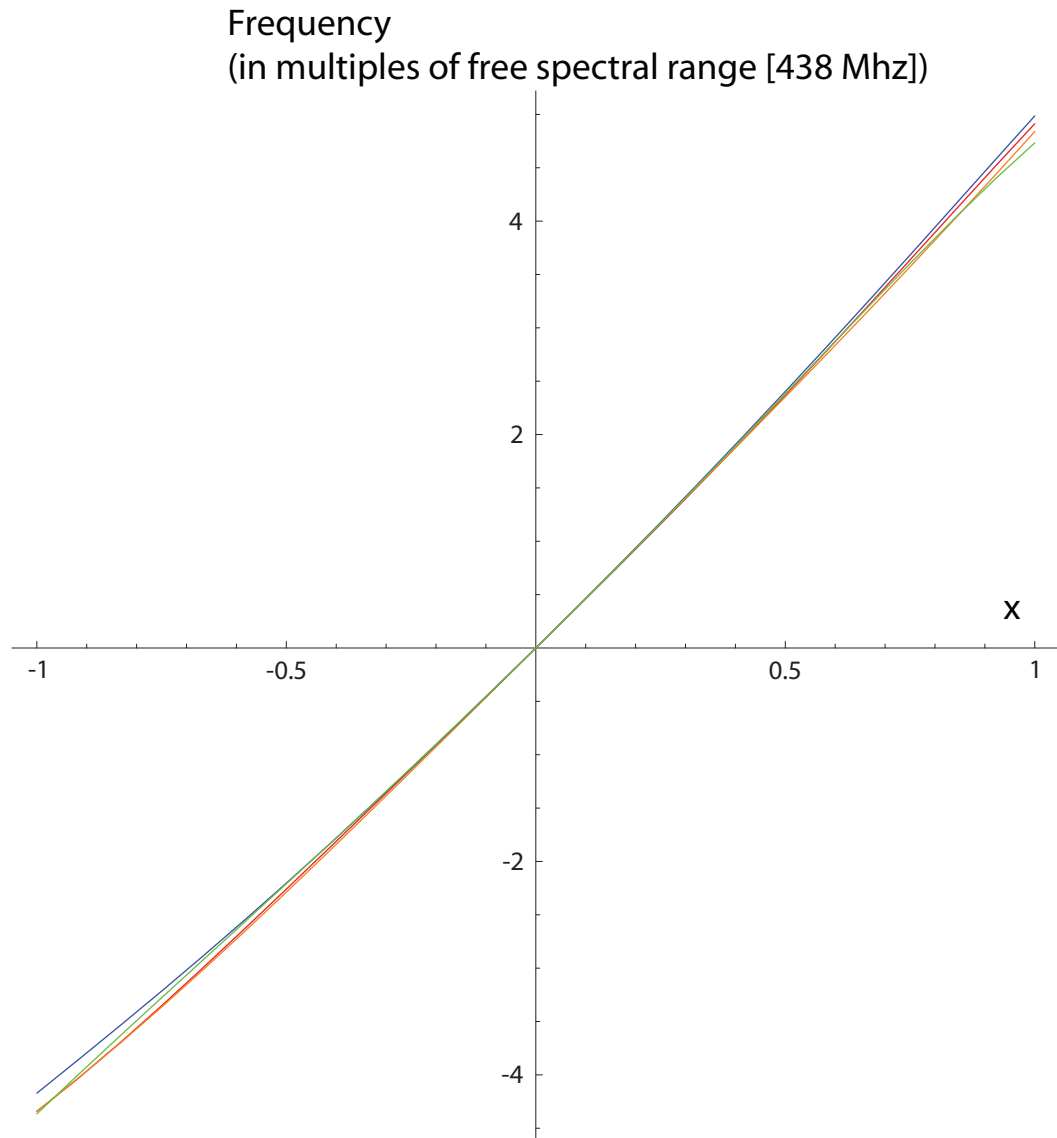


Figure 5.3: Four calibration scans demonstrating the nonlinear relationship of voltage (rescaled to x) and frequency. Two of the scans (blue and green curves) start a low voltage and move to a higher one (up scans) and the other two scan the opposite direction (down scans). Hysteresis can be noticed upon close examination.

Chapter 6

Future Work

6.1 Conclusions

The work detailed in this thesis has augmented and refined an experimental system that is ready to yield results. Improvements to the cavity locking, laser locking and optical systems are complete as described in the following appendices and preceding chapters. The experimental system is a preliminarily complete and robust setup. A flexible procedure and supporting software for calibrating the frequency of the laser are finished. Software for acquiring data and controlling electronics in the apparatus has been developed and tested.

The research is presently in the stage of identifying and improving the differential phase shift signal in the atomic beam apparatus. A number of steps that should be taken next are outlined below.

6.2 Detecting and Optimizing the Experimental Signal

The scheme for identifying the signal thus far is:

- Optimize the power transmitted through the ring cavity by the weaker frequency shifted (CCW) beam while scanning the cavity. (Optimal peak values range around 600 mV for the New Focus photodetector with a preamplifier gain of 10^4).
- Attenuate the unshifted beam (CW) to match the amplitude of the shifted beam. (Again, the peak value should be around 600 mV).
- Stop scanning the cavity and lock to the inflection point of the CW beam. Optimize the differential signal as described in section 4.3.
- Scan the laser over about a half gigahertz at a rate less than a hertz using a sine function (to prevent the cavity locking system from bumping out of lock

on the sharp transition of a triangle wave). A better scanning function would be a triangle wave with the peaks smoothed, which could be accomplished with the computer. Center the scan over the transition (around 233612.7 GHz) by manually adjusting the DC offset of the laser PZT. Feedback this laser scanning signal to the cavity PZT using the summing amplifier described in section 3.6.

- Adjust the time constant of the cavity PID controller and manual tuning of the cavity PZT to allow the cavity to remain locked. The PID controller will have to produce a sinusoidal correction signal to compensate for the correction the summing amplifier is not completely providing. Adjust the laser scan gain control on the summing amplifier to minimize the correction signal of the PID controller.
- Increase the laser scanning rate to 2-5 hertz and the range to around 2 gigahertz and again adjust the PID time constant to maintain locking while scanning.
- Turn on the atomic beam and look for the expected experimental signal on the differential output.

It is not presently clear that the atomic beam is properly producing atoms, and the operation of the atomic beam must be verified and corrected if necessary. Once this is accomplished, the technique above can continue initially to be used to identify the signal. It will be necessary to continue to improve the noise on the differential signal as the experimental signal expected is quite small. Several possibilities exist for further optimizing the differential signal:

- Investigate the delay between the two photodetectors before they enter the differential amplifier. Even a slight difference in delays could decrease the quality of the common mode noise rejection. A possible solution would be to replace the two discrete units with a single unit with two inputs and built in differential circuitry (and equal delays). This was attempted in the present work with a New Focus 2117 balanced receiver, but the unit was defective as the amplifier produced excessive high frequency noise on high gain settings.
- Improve the quality of the locking while scanning system by introducing an adjustable delay in the signal going to the laser PZT and the identical signal going to the summing amplifier (and then to the cavity PZT). The response of the laser PZT and the cavity PZT are not synchronized; thus, the PID controller still has to provide a fairly large correction signal simply to mitigate the effects of the laser scan (see section 3.6 for further details on the reason this correction is needed). By introducing an adjustable delay, the correction signal sent to the cavity PZT by means of the laser scan signal could more fully account for the correction needed and thus allow the PID controller to do less work. This will likely lead to a more robust lock and perhaps a cleaner signal.

Once the signal has been identified, slower scans using the computer software developed for this purpose (see section D.4) can be used to collect data and average over appropriately long times.

6.3 Isotope Shift Measurement

The next step after identifying the signal will be to measure the isotope shift (see section 2.2 for details on the effect). The apparatus will not need to be modified much, if at all, for this measurement. A section of the laser beam will be diverted into an external Fabry-Perot cavity in order to run calibration scans at the same time the ring cavity differential signal data is being collected. This will allow for precise frequency calibration of the atomic data as discussed in chapter 5 and appendix C. The amplitude of the signal as a function of frequency will not be crucial here as the frequency spacing is the subject of interest.

6.4 Stark Shift Measurement

To measure the Stark shift in this transition, electric field plates oriented so that the electric field is in the \hat{z} direction will need to be installed. The plates already exist from use in earlier Stark shift measurements (in the 378 nm transition), and installation should be straightforward. The top plexiglass plate of the cavity shield (that protects the mirrors of the ring cavity from stray thallium) will have to be removed. The top electric field plate will serve this protective role in this case. See figure 6.1 part a for the configuration of the electric field in relation to the atomic beam and ring cavity for the Stark shift measurement.

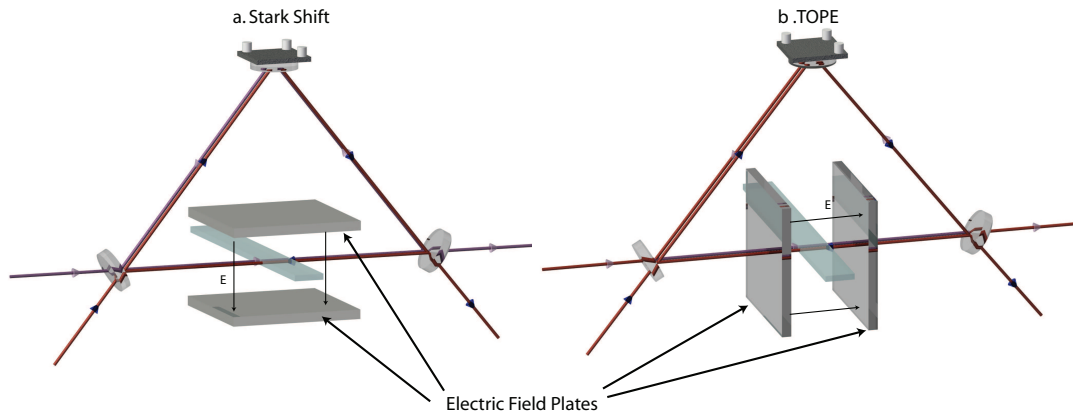


Figure 6.1: Configuration of the ring cavity necessary for the future Stark shift (a) and TOPE (b) experiments.

6.5 TOPE Experiment

Once the above steps have been accomplished, the transition to the TOPE experiment should not be particularly difficult. The tricky apparatus change that will need to be made is the construction and installation of a set of electric field plates that produce an electric field parallel to the laser beam (see figure 6.1). As the beam will necessarily have to pass through these plates, they will have to be constructed in one of two ways:

- Transparent plates could be made (at great expense) with antireflection coatings such that the laser beam could pass through unimpeded but a charge could still be placed on the plates. The major disadvantage to this option (besides the cost) is that inserting a new surface, however transparent and well AR coated it may be, degrades a laser beam. In the environment of the Fabry-Perot ring cavity where each beam makes many trips around, this could be a serious issue.
- A small hole (less than a millimeter) could be made in more traditional metal electric field plates to allow the beam to pass. While the disadvantages of the first method are avoided, this introduces a different problem. The small holes will produce a complicated electric field as the plates are no longer two infinite planes of charge (infinite at least as far as the field at the center of the plates is concerned). A possible way to mitigate this effect would be to augment the area around the holes with more metal to compensate for the holes in such a way that the field at the center was equivalent to that of two plane charges. This would make an excellent modeling project for a future student.

The AOM and related optics that frequency shift one beam will be removed, as both beams will need to be at the same frequency (since the differing directions of the beams will produce a nonzero differential signal if a TOPE force exists). Software will need to be written to handle data collection, perhaps also controlling the stepper motor to block and unblock the atomic beam. This will allow for background (atom free) scans to be taken interleaved with data scans. At this point, the information gathered in the above experiments will guide the future of this work.

Appendix A

Ring Cavity Locking Hardware

A.1 Scanning the Laser Frequency

The laser source in these experiments is a Newport diode laser in an external cavity configuration where a tunable diffraction grating selects and feeds back a fraction of the diode's output (illustrated in figure A.1). The frequency that is fed back is then amplified by stimulated emission and is emitted to the rest of the experimental system. This configuration allows single mode operation of the laser and fine control of the frequency by setting the voltage applied to a stack of piezoelectric transducers (PZT) that controls the tilt of the diffraction grating.

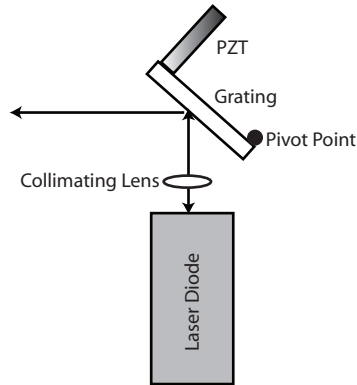


Figure A.1: Laser Configuration: the laser diode emits a broad frequency spectrum from which a single frequency is selected for stimulated emission by the position of a PZT controlled diffraction grating.

In August 2006, the laser refused to tune when a voltage was applied to the PZT. The failure was identified as a short in the PZT. This short destroyed the current PZT control electronics, which consisted of a manually tunable offset that was added to an external signal which could be driven by a computer or function generator. The old PZT, which was salvaged from a nonfunctioning laser, bore the label 8A618 and was

approximately 6 mm x 6 mm x 20 mm in size. As the exact make of this PZT could not be determined, it was replaced by a ThorLabs AE0505D18 piezoelectric stack (manufactured by Tokin Corporation, see figure A.2), which has similar dimensions. The ThorLabs PZT was installed and wired to a new control box that allows the same manual tuning of a DC offset that is then added to an external signal (which is first amplified ten times). The new PZT can take voltages ranging from 0-100V; it is imperative that the PZT not be given a negative voltage, or it will be damaged. The laser was reassembled and retuned manually to lase at 1283 nm when the PZT was set at $\sim 50\text{V}$, thus giving a good tuning range below and above the transition. After the repair the laser operated as well or better than before the repair in terms of tuning range ($\sim 20\text{ GHz}$) and frequency stability.

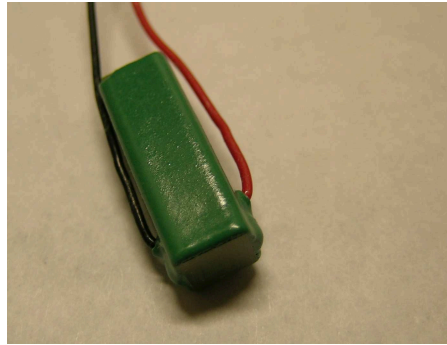


Figure A.2: ThorLabs AE0505D18 PZT used to replace the defective stack in the experiment's diode laser.

A.2 Hardware

The cavity locking system was upgraded with the addition of a new PID controller and a summing amplifier that allows long scans of the laser to be made while maintaining cavity lock (as discussed in section 3.6). An image of the summing amplifier is provided for reference in figure A.3. The present state of the cavity locking system is diagrammed schematically in figure A.4 to facilitate understanding of the somewhat complex network of equipment.

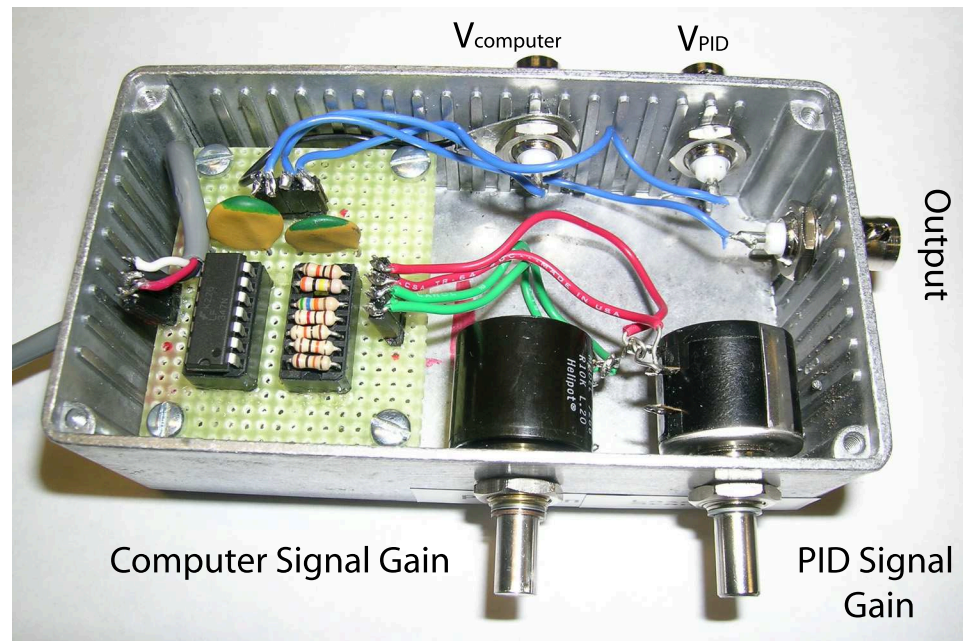


Figure A.3: Final prototype of the Summing Amplifier.

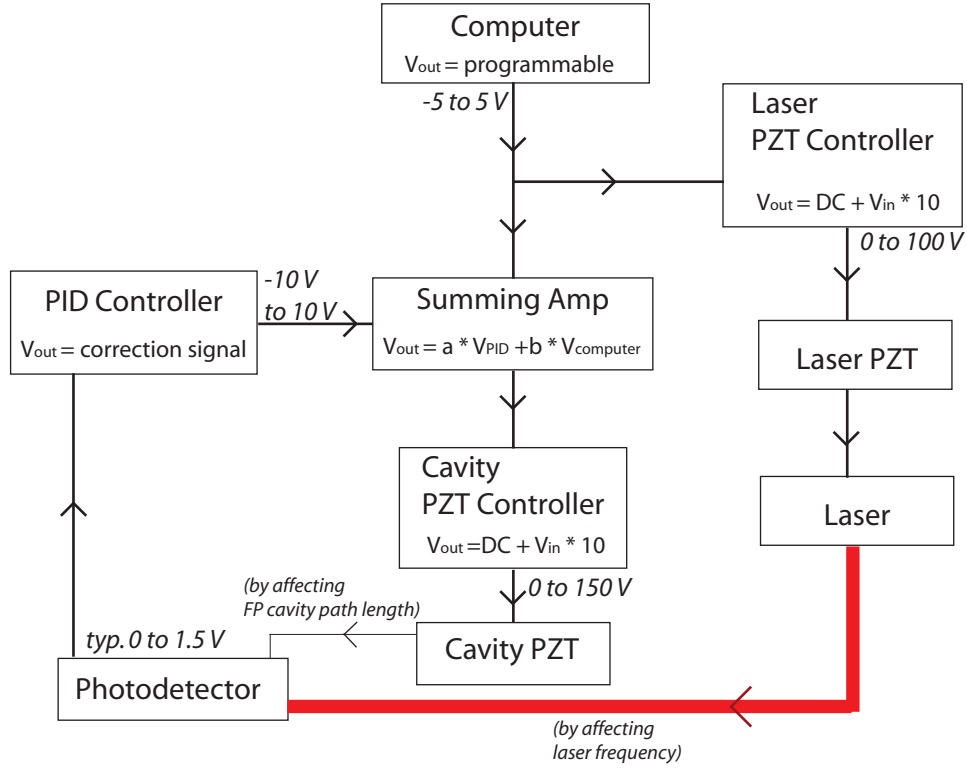


Figure A.4: Block Diagram of the present cavity locking system. Note: the values for the summing amplifier preamp coefficients: a can be tuned from 0.001 to 0.01 and b can be tuned from 5 to 10. This can be directly calculated from the resistors used in figure 3.8. Also, the laser and cavity PZTs are not physically connected to the photodetector; rather, they affect the laser frequency and cavity path length which in turn changes the signal on the photodetector.

Appendix B

Laser Locking Hardware

As discussed in section 3.7, the laser locking system uses Faraday rotation caused by Zeeman splitting of the thallium energy levels to stabilize the frequency of the laser.

B.1 System Improvements

B.1.1 Oven

To achieve the vapor pressure necessary to study this weak M1 transition, it is necessary to heat the thallium cell to roughly 800°C. Achieving and maintaining such high temperatures is technically challenging. Furthermore, the thallium vapor cell is placed in an evacuated ceramic tube at ~ 5 torr to minimize noise caused by air convection at the interface of the hot oven and the substantially cooler room air. During the course of the past year, both the electrical distribution system for the heating elements and the vacuum tube failed and were consequently repaired and improved to lower the chances of future problems.

The oven consists of an outer cylinder of μ -metal filled with fiberglass insulation, an inner aluminum cylinder wrapped in copper wire to create a solenoid and a ceramic tube containing the thallium vapor cell (figure B.2). The ceramic vacuum tube is surrounded by four clamshell heaters (Mellen 126-3006: 3 3/4" ID, 825 W, 115V). The configuration forces the center of the vapor cell to be slightly cooler than the ends, preventing buildup of metallic thallium on the ends of the vapor cell which would block the laser light. The clamshell heaters are not driven by standard AC current as that would create 60 hertz magnetic fields which is manifest as noise in the resulting polarimeter signal. Rather, the heaters are driven at ~ 18 kilohertz, sufficiently higher than our signal so that the lock-in eliminates the noise effectively. A function generator drives four audio amplifiers (Gemini GXA 1600), which in turn are connected to the heating elements. Four switches and four coaxial connectors are provided to allow temporary disconnection of an element and monitoring of the driving current respectively. These elements of the electrical distribution have not been substantially modified and are robust.

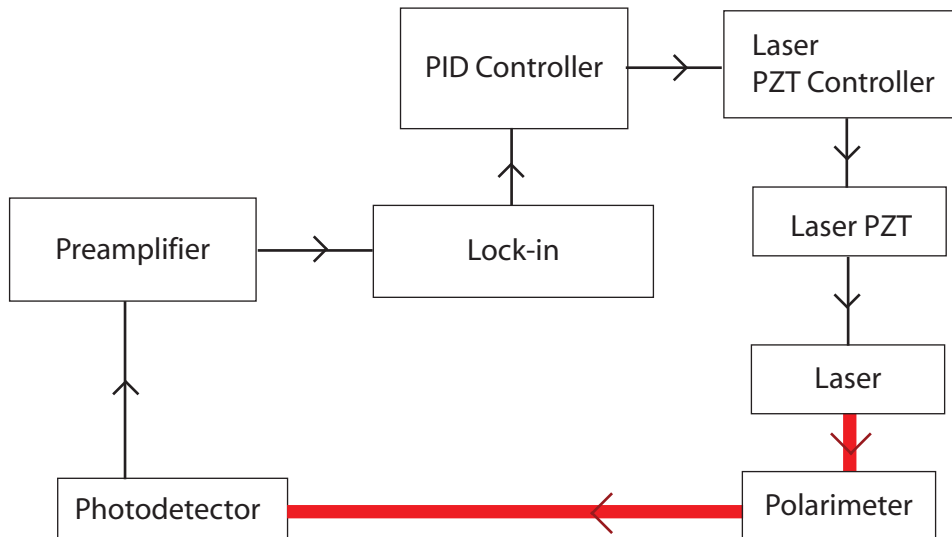


Figure B.1: Block Diagram of the laser locking system.

However, the connections from the front panel (switches and coaxial connections) to the heater element leads must occur inside the oven due to the short length of the heater leads (see figure B.3). The combination of high current (4-5 rms amperes) and high temperatures require careful connection design. In August 2006, the oven failed to reach temperature (800°C). The failure was traced to these connections in two of the oven elements. Three working elements are sufficient to reach temperature if the amplifiers are driven at maximum without clipping, but it takes many hours; two elements are insufficient to reach temperature. Thus, slow heating is an indication of failure of a heating element even if the oven is capable of reaching temperature eventually; the offending element should be repaired in this case. The heater elements have an internal resistance of ~ 16 ohms which can be tested by an ohmmeter for quick identification of the failed connection. When all four elements are functioning properly, it takes ~ 3 hours to reach 800°C.

The heater to exterior connections are two plates of aluminum roughly 3 cm by 10 cm connected by two 1/4-20 bolts. These plates are tightened onto the heater leads and external wire, one at each end. The large surface allows for good positive contact between the wires (see figure B.4). The failures discussed above occurred where the heat from the oven, combined with the high current, corroded the external wire at the point where it met the aluminum plate, essentially building a layer of resistive material between the metal plate and the wire. This problem seemed to be particularly pronounced on the north end of the oven, where copper wire was used for the external connections. The corrosive material was removed and the aluminum

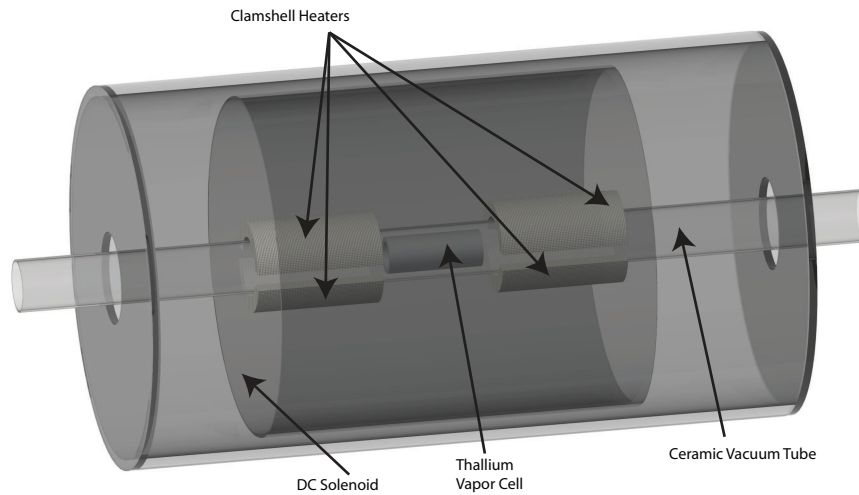


Figure B.2: Basic parts of the Laser Locking Oven. Materials rendered transparent for ease of view.

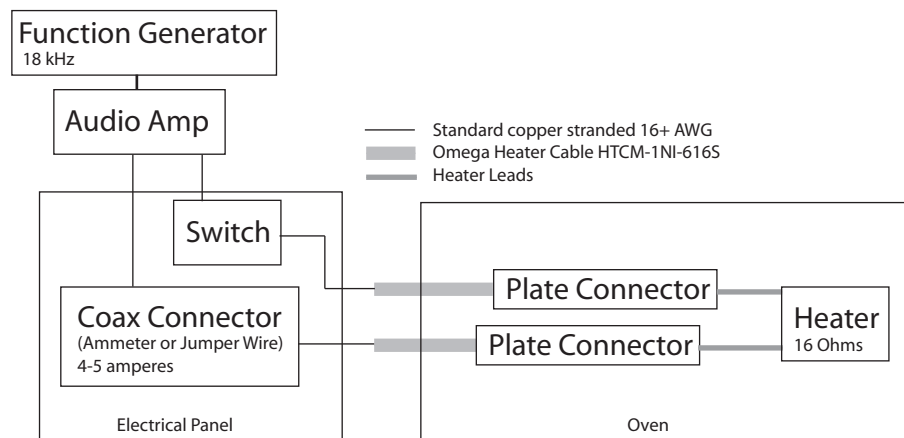


Figure B.3: Electrical circuitry for powering a clamshell heater elements. This circuitry is duplicated four times for all the heaters (N1, N2, S1, S2).

plates sanded clean. The problem reoccurred in February 2007, and the copper external wire was replaced by nickel core cable rated for oven use (Omega HTCM-1NI-616S: 16 gauge, 600 V, 1000°C) on the north side. The south side of the oven already has nickel core wire and thus has experienced less difficulty with this corrosion issue; in the event these connections fail, enough Omega wire has been procured to refit this side as well.

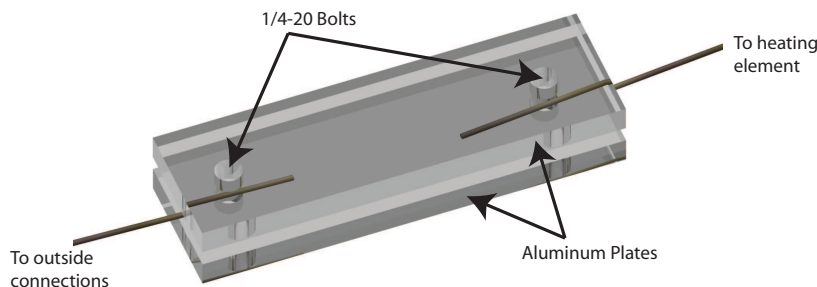


Figure B.4: Diagram of connectors for heating element leads to external routing cable. Plates are aluminum (again shown transparent) and contacts are dry, as solder would melt in the oven environment.

The vacuum system is comprised of two aluminum end caps that tighten onto rubber O-rings to form a seal onto a hollow alumina ceramic tube as shown in figure B.5. The vapor cell is placed in the center of the ceramic tube on a mount for stability. Two thermocouple wires are run through to the center of the tube to provide measurements on the temperature at the center and end of the vapor cell. In December 2006, the ceramic vacuum tube (3.325" OD, 3.075" ID) experienced a complete fracture in about the center. The cause of the fracture is not precisely known; it was likely due to repeated heating and cooling cycles over a long period (~ 8 years). The 54" tube was replaced with an alumina tube with similar outside dimensions so that the same end caps could be used. However, the replacement tube (CoorsTek 66473: 3.25" OD, 2.875" ID) had a wall thickness of $1/4$ ", twice the thickness of the broken tube. The increased thickness should lead to better structural strength, even though the tube should be subject to minimal force beyond its own weight. The end caps were successfully replaced with smaller O-rings (size 338). The resulting vacuum was of better quality than before the repair (less than 5 torr). The vacuum was maintained at better than 20 torr over a period over two weeks, far better than before the breakage, where the vacuum would hold at that level for less than a day.

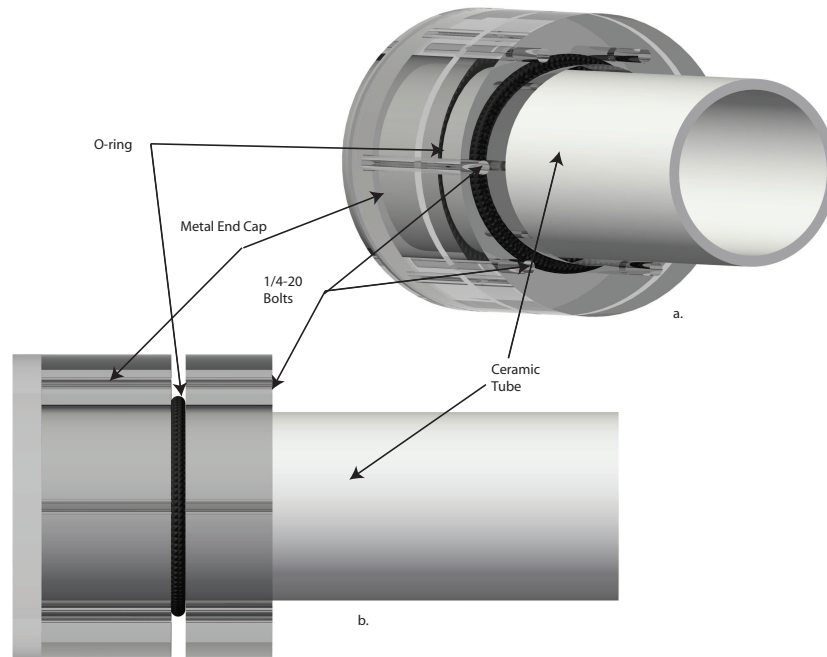


Figure B.5: Isometric view (a) and side view (b) of the vacuum tube end caps. Bolts tighten the two aluminum parts (shown transparent here) onto an O-ring to make a seal against the ceramic tube. Not shown is the connection to the vacuum pump (north cap) and thermocouple inputs (south cap).

B.1.2 Faraday Rotator

The original AC solenoid responsible for the magnetic field inside the high Verdet constant glass rod had no mechanism for dissipating heat, and thus the glass rod and surrounded air would reach unacceptably high temperatures. Keeping the glass and air cooler was expected to reduce the noise in the laser and allow the locking system to be used faster from a cold start. Previously, the solenoid had to be allowed to come to temperature before final alignment of the optics. In the current work, a water cooled solenoid was designed to create a similar magnetic field while transferring far less heat to the air and glass. As the oven was already water cooled, the water distribution caused little difficulty. The first prototype was manufactured out of aluminum for its excellent thermal conductivity and wrapped with AWG 26 magnet wire. Unfortunately, in use, no detectable AC magnetic signal was found inside the glass. The obvious electrical conductivity had not been adequately considered, and thus the ~ 700 hertz AC magnetic field was completely countered by eddy currents in the aluminum before it came anywhere near the center of the solenoid where the glass resides! The problem can be analyzed mathematically by considering the skin depth. The skin depth is the distance before a signal is attenuated by $1/e$ and is defined as

$$d \equiv \frac{1}{\kappa} \quad (\text{B.1})$$

where

$$\kappa \equiv \omega \sqrt{\frac{\epsilon\mu}{2}} \left[\sqrt{1 + \left(\frac{\sigma}{\epsilon\omega} \right)^2} - 1 \right]^{1/2} \quad (\text{B.2})$$

For aluminum with a signal of 700 hertz, $\omega = 4400$, $\epsilon \approx \epsilon_0$, $\mu \approx \mu_0$, $\sigma = 3.77 \times 10^7$ [Gri99]. By equations B.1 and B.2, $d = 3.0$ mm. The thickness of this prototype solenoid was 15.9 mm. Clearly, the aluminum would not be satisfactory for generating any magnetic field in the glass rod. The same design was then machined in plexiglass, which has a high resistivity, eliminating the skin depth problem. The resulting solenoid (again wrapped with AWG 26 magnet wire with a total resistance of ~ 8 ohms) has good thermal properties and is now part of the experimental setup.

B.1.3 SRS SIM 960 PID Controller

As mentioned above, the processed signal from the lock-in is sent to a PID controller which is set to lock on the zero crossing of the dispersion curve. The setup was upgraded to make use of a commercial PID controller (SRS SIM 960) in place of the older homebuilt box. This is an identical unit to the PID controller that locks the Fabry-Perot ring cavity. The new unit gives more flexibility in setting the parameters such as proportional gain, integration time constant, and so on. The laser locks well with a proportional gain setting of 0.1 and an integration time constant of $2.0 \cdot 10^2$ 1/s. This proportional gain setting is the minimum on this controller, but it is possible to further lower the effective gain by reducing the sensitivity of the photodetector

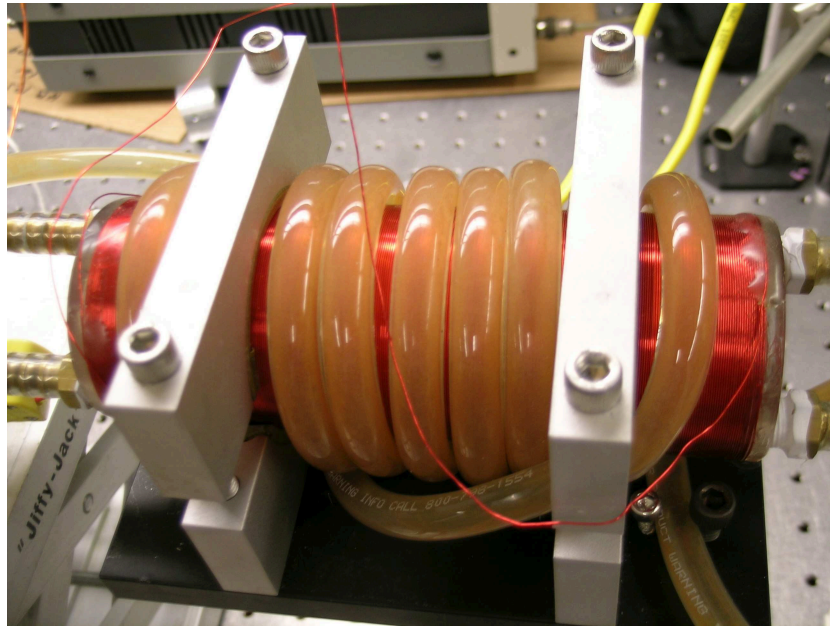


Figure B.6: Final prototype of the new water cooled solenoid and mount for creating an AC magnetic field in the polarimeter's glass rod.

amplifier or the lock-in. Increasing the time constant (which is displayed in inverse seconds in this PID controller) reduces the sensitivity of the PID controller to transient noise spikes that can bump the system out of lock, but it also reduces the bandwidth and the ability to make fast corrections.

This PID controller allows for computer control through RS-232 or GPIB interfacing. Either interfacing protocol can be used by LabVIEW, allowing control of the PID controller to be integrated into the current data acquisition and control software (see appendix D).

B.2 Laser Locking Procedure

The procedure of locking the laser from a cold start is slightly complicated, therefore it is helpful to have a checklist to follow.

- Turn on the oven by switching on the audio amplifiers, and let it stabilize at $\sim 800^{\circ}\text{C}$ (several hours).
- Manually tune the laser near the transition using the wavemeter as a guide. Input a function generator running at less than a hertz to the laser and adjust it to scan around the transition.
- Turn on the photodetector preamplifier, lock-in, Faraday rod solenoid power

supply, function generator ($\omega_m \approx 700$ hertz), and ammeter. Set the power supply to provide about 2 amperes.

- Trigger on the solenoid function generator and look for the signal on the photodetector. Manually tune the angle of the analyzer polarizer until only the signal at $2\omega_m$ and there is no ω_m component. Adjust the alignment of the optics until the signal (peak to peak) to background ratio is about one.
- Turn on the solenoid for the thallium cell at 1.5 amperes. Put the oscilloscope in XY mode with the function generator driving the laser as X and the lock-in signal at ω_m as Y. The Faraday rotation lineshape should be visible.
- Replace the function generator driving the laser PZT with the PID controller. Manually tune the PID controller near the zero crossing of the dispersion curve and start locking. The gain on the preamp or lock-in may need adjusting to preventing overdriving of the lock, which is manifest as a circle on the oscilloscope in XY mode.
- Check for a robust lock by changing the internal setpoint of the PID controller. The lock location should visibly shift accordingly.

Appendix C

Laser Scan Calibration: Technical Details

The calibration technique described in chapter 5 is coded in MATLAB, which is a programming language specific to the MATLAB technical computing environment (published by The MathWorks). MATLAB is a high level language with similarities to C and Java but with greatly enhanced capabilities to manipulate large data sets (in matrices) in single instructions. This makes the language much more useful for data analysis than C, Java or Mathematica. The functionality of the language can be expanded with add on libraries (toolboxes); the work presented here makes use of the curve-fitting toolbox.

C.1 Data Preprocessing

The input to the fitting routine is a data file from one of the LabVIEW data acquisition programs described in appendix D. Due to the limited mathematical abilities of LabVIEW, the data is not processed at all, but is merely written directly to a tab delimited text file with a header containing information about the scan. Before fitting an airy peak, the raw data file from LabVIEW must be processed to find the mean and standard error for each voltage sent out to the laser PZT. This is done by the MATLAB routine *LaserScanPostProcessor.m*.

LaserScanPostProcessor.m prompts for an input file ***filename*** and outputs to a new file **mean_se_*filename***. The program execution is linear and requires no further user input:

1. **Copy** out header into new file **mean_se_*filename***. Store number of samples at each voltage interval as N .
2. **Find** the end of header as marked by line **End of Header – Data follows:**. The following line is assumed to be tab delimited column titles in the form:

independent variable *tab* dependent variable 1 *tab* dependent variable
2 ...

3. **Read** in these column headers.
4. **Calculate** the mean and standard error ($\frac{\sigma}{\sqrt{N}}$) for each dependent variable (which are typically voltage readings from a photodetector).
5. **Output** new column headers to the new file **mean_se_filename** in the form:

independent variable *tab* dependent variable 1 mean *tab* dependent
variable 1 standard error *tab* dependent variable 2 mean *tab* depen-
dent variable 2 standard error ...
6. **Output** data in the same tab delimited form as the new header.

Here is an example of the first portion of a raw data file,
CWFabryPerotScan14(up).txt, before processing with
LaserScanPostProcessor.m:

```

Majumder Lab Data
2007-01-18 15:22
Fast scan of laser looking at CW Fabry Perot Peaks
Zero point on Piezo controller is 64.2 - 233612.8
-1 V is 233608 GHz
+1 V is 233618 GHz
Sample Rate (Samples/Second): 1000
Number of Samples/ Voltage Interval: 10
Start Voltage Out: -1.000000
End Voltage Out: 1.000000
Voltage Out Step: 0.001000
Stepping Time (Seconds): 0.000000
Channel 1 In: ai0
Channel Out: ao0
End of Header -- Data follows:
Voltage Out{tab}CW
-1.000000E+0{tab}5.095889E-3
-1.000000E+0{tab}3.963113E-3
-1.000000E+0{tab}1.626182E-2
-1.000000E+0{tab}5.257714E-3
-1.000000E+0{tab}3.963113E-3
-1.000000E+0{tab}3.639463E-3
-1.000000E+0{tab}3.425014E-1
-1.000000E+0{tab}6.552314E-3
-1.000000E+0{tab}3.963113E-3
-1.000000E+0{tab}2.830338E-3
-9.990000E-1{tab}4.124938E-3
...
```

This is the first portion of the processed data file,
(**mean_se_CWFabryPerotScan14(up).txt**):

```
Majumder Lab Data
2007-01-18 15:22
... {same header as above} ...
End of Header -- Data follows:
Voltage Out{tab}CW Mean{tab}CW Std Error
-1{tab}0.039403{tab}0.03197
-0.999{tab}0.014466{tab}0.0033363
-0.998{tab}0.068661{tab}0.04638
-0.997{tab}0.007944{tab}0.00053043
-0.996{tab}0.008656{tab}0.00013147
-0.995{tab}0.0087855{tab}8.8042e-005
-0.994{tab}0.0092224{tab}0.00030383
-0.993{tab}0.010112{tab}0.00030188
...
```

C.2 Airy Function Fitting

The file produced by *LaserScanPostProcessor.m* can now be used by the Airy function fitting routine *Fit_Airy_Version1_1_07tes.m* to generate values for the coefficients $a_0, a_1, a_2, \dots, b_0, b_1, b_2$, etc. as described in section 5.2.

The program execution of *Fit_Airy_Version1_1_07tes.m*¹ is also linear and requires no user input beyond choosing the file to fit:

1. **Prompt** for file or files of form **mean_se_*** (preprocessed data file) containing an Airy function to be fitted.
2. **Locate** peaks in the Airy function. The location algorithm establishes a threshold of 0.3 times the maximum height. Any amplitude values below the threshold in the data set are replaced with zero. This eliminates any miniature peaks caused by noise in the data. Then, the algorithm starts at $x = -1$ and looks for nonzero values in the data. When it finds one, it flags a peak start found at that x value. Then, it looks for the next zero value. When it is found, this data point is considered a peak stop. A peak value is recorded for the mean of the peak start and peak stop. The remainder of the peaks are found in this fashion. See figure C.1.
3. Based on the frequency spacing between two peaks, guess a value for the linear coefficient a_1 . **Perform** a nonlinear least-squares fit of equation 5.3 to the peak values found by examining the data. This gives preliminary values for

¹Another program, *Fit_Airy_Version1_07tes.m* is identical in execution but only handles a single file at a time.

a_0 through a_6 . (The current version of the program fits up to the x^6 term, which is insignificant, but including it helps the quality of the fit). If the data contains fewer than seven peaks, only the linear and quadratic coefficients are fit preliminarily (a_1 and a_2). Prompt the user to check to ensure the preliminary fit is reasonable. See figure C.2 part a.

4. Using the preliminary guesses for the coefficients obtained in the previous step, **fit** the entire Airy function (equation 5.4) to the entire data set. Prompt the user to ensure the final fit is reasonable. Occasionally, fits will not work, but these are readily apparent by a curve that does not match the data at all. See figure C.2 (b).
5. **Repeat** the preliminary and final fits for all the files selected by the user initially. **Output** data containing the coefficients and goodness of fit for all the files to the screen and to a user selected file.

This routine is fairly robust and automated so that it could operate as a subroutine for a larger program that could take an atomic scan and its corresponding calibration Fabry-Perot scan, fit the calibration scan to an Airy function as described above, generate a correction for the atomic scan and output an atomic scan with a calibrated frequency axis. The two programs described above are well documented, if the user or future programmer requires more information than is contained in this appendix.

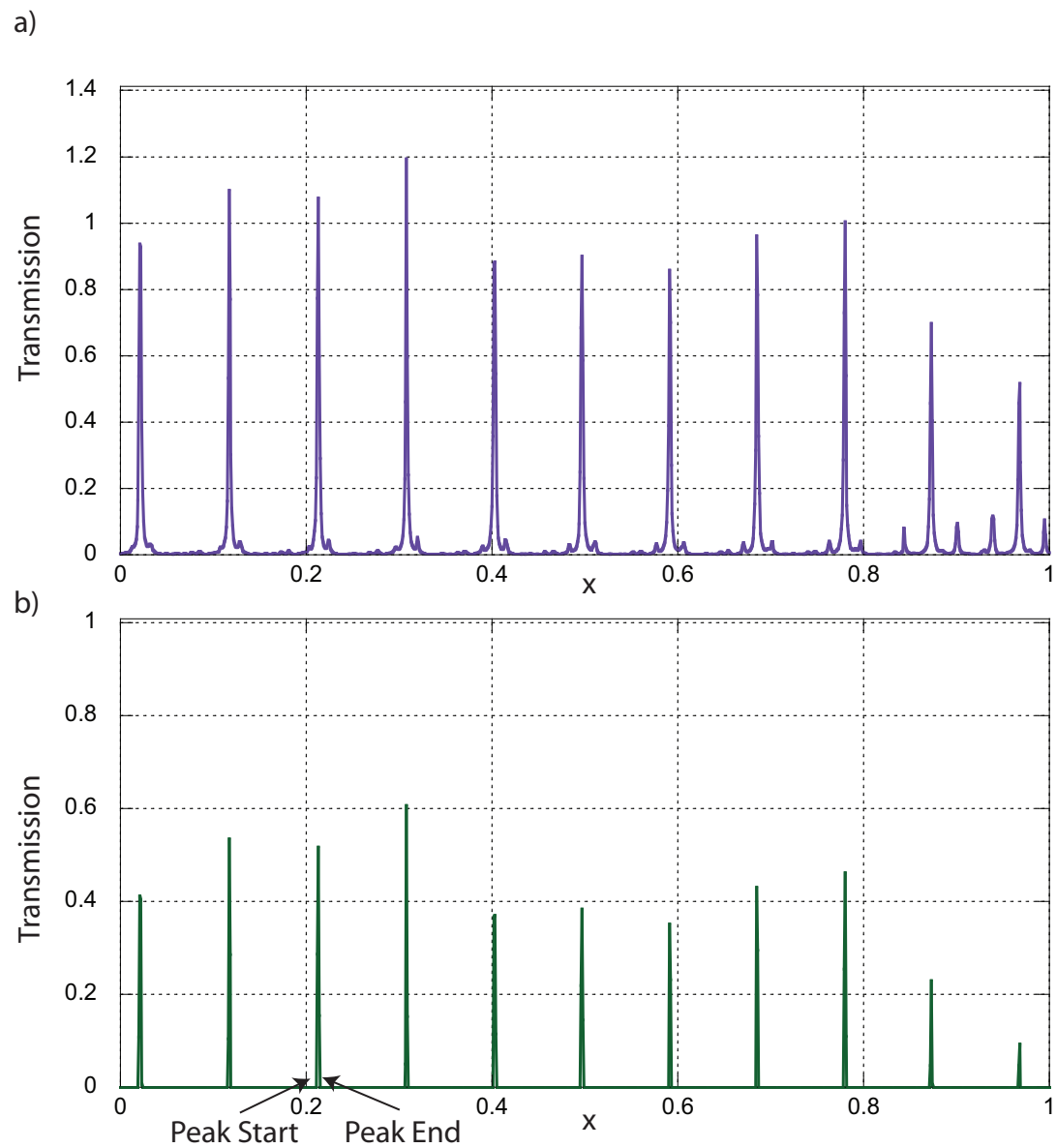


Figure C.1: Graphical demonstration of the peak location algorithm on actual data. a) shows the raw data and b) shows the data after rejecting values below the threshold.

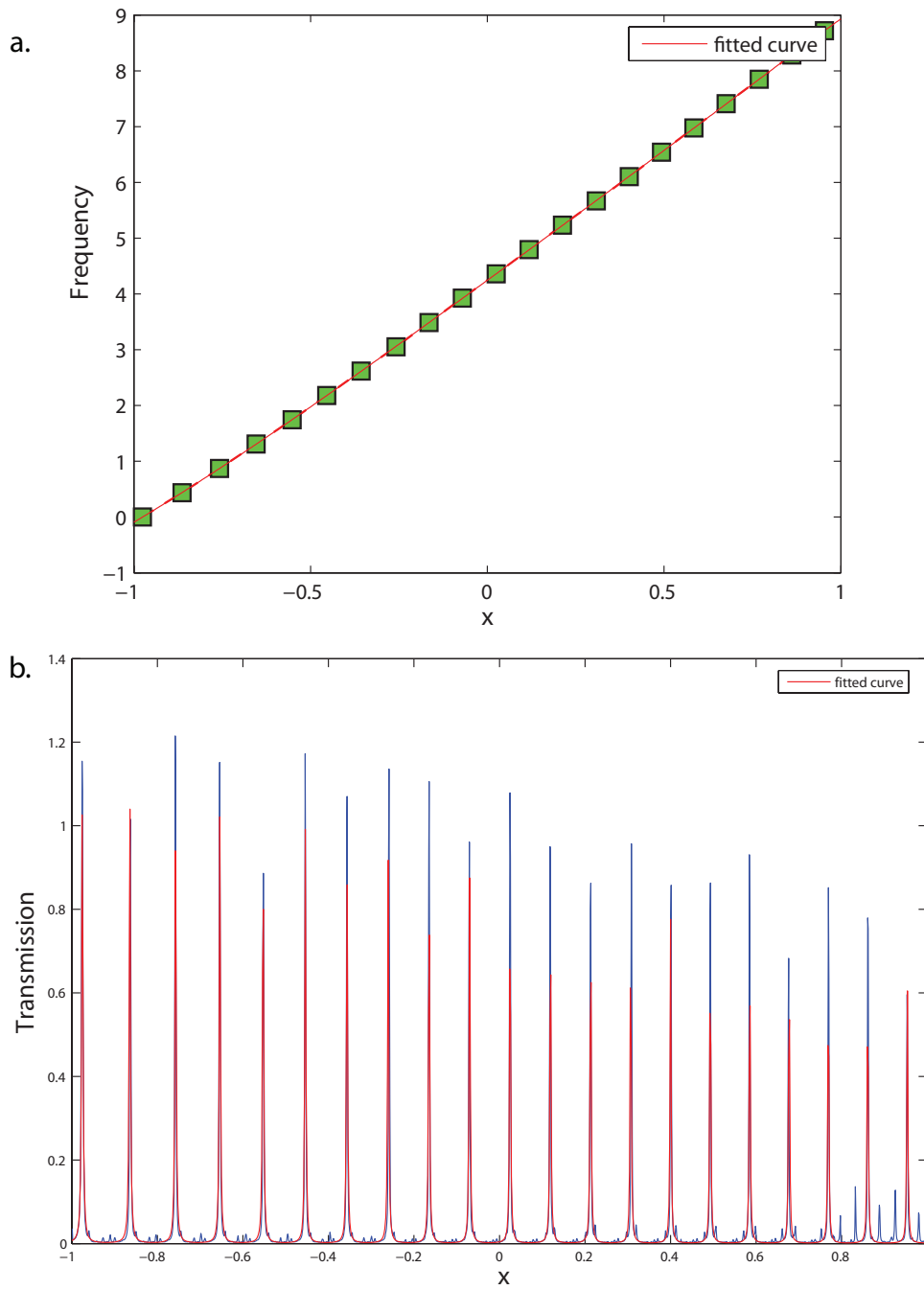


Figure C.2: Graphs provided to user by *Fit_Airy_Version1_1_07tes.m* to validate a successful prefit (a) and final fit (b).

Appendix D

Acquisition and Control Software

The data acquisition and system control software was in serious need of upgrading, as the computers and relating hardware were obsolete. To replace this aging equipment, an Apple G4 Macintosh running Macintosh OSX and National Instruments' (NI) LabVIEW graphical programming language (version 7.1.1) was installed. To interface the computer with the lab equipment with BNC connectors, a NI-DAQ (National Instruments DATA acQuisition) M series card (PCI-6221, 68 pin) was installed in the computer and routed to a breakout box with BNC connectors. This NI-DAQ card allows for three ports of eight lines each of digital input/output, sixteen analog inputs, and two analog outputs. The ADCs in this card allow 16 bit resolution. A PCI GPIB card was also installed in this computer to control devices with GPIB control.

D.1 A Graphical Programming Language

LabVIEW is a member of a unique class of programming languages that work by drawing connections (wires) between graphical subunits (virtual instruments or VIs). Each VI has a specific function and requires inputs in the form of wires of the correct data type (number, string, boolean, etc.). A VI might have a simple function like adding two numbers or a complex one like operating hardware to collect data for an entire range of values. VIs are analogous to functions and subroutines in traditional text based programming languages. LabVIEW has the advantage of being quite quick to use once the user has mastered the rather different style of programming. It handles the low level hardware control such as GPIB, serial or DAQ card interfacing with minimal work from the programmer.

However, with this high level of abstraction, a good deal of efficiency is lost. The programmer also has little knowledge of how the program is implementing certain features, making optimization difficult. The graphical programming style makes good programming style difficult. When modifying VIs, rather than inserting in new lines of code, the programmer must clear screen space to fit the new VIs and wires in. Clean programming is much harder as well, as the wires and VIs have a tendency to get messy. To keep the back panel (i.e. code) clean, the programmer is encouraged

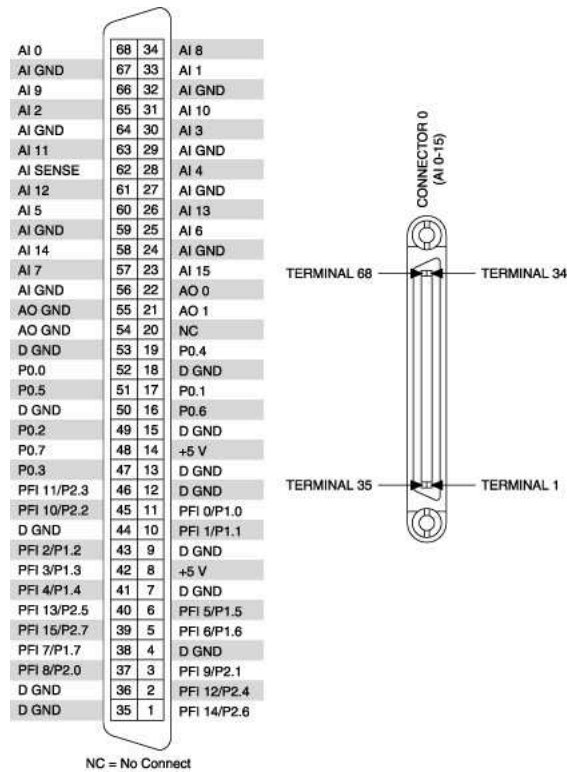


Figure D.1: Pinout of the NI-DAQ PCI-6221 card. AI is analog input, AO is analog output, *Pport.line* is a digital line configurable in software as input or output. [Nat05]

to use many subVIs: VIs that are called by the main program (also annoyingly called a VI). By careful use of subVIs to perform jobs needed by the main program, the graphical code can be kept tidy, which is essential for future readability. Commenting code is also much harder; make use of the text box tool. A further drawback of LabVIEW's graphical programming is that useful techniques like recursion are not possible. Performing mathematics and plotting is complex, and it is advisable to use a program like MATLAB for such tasks. Once the programmer keeps these limitations in mind, LabVIEW is a useful and powerful tool for developing computer control and data acquisition software.

D.2 Data Acquisition with the NI-DAQ PCI 6221

All of the software described below makes use of the NI-DAQ PCI 6221 card. The process of reading and writing from this hardware within LabVIEW is somewhat non-intuitive, so the basics are outlined here before proceeding to the specific programs. All I/O through the card, whether digital (TTL) or analog ($-10\text{ V} \rightarrow +10\text{ V}$) requires a similar sequence of VIs:

1. DAQmxBase Create Task: requires no inputs and creates a task, which is basically a purple wire that carries the information about this I/O operation from VI to VI throughout the program. This VI also has an error output like all the DAQ VIs. This output can be ignored, as will be done here, if explicit error handling is not needed. DAQmxBase is just National Instruments' name for the software that interfaces the NI-DAQ card to LabVIEW.
2. DAQmxBase Create Channel: requires two inputs: a task (generated by Create Task) and a string specifying a physical device and channel name. The latter input is formed by the device name which will be *dev0* assuming only one NI-DAQ card in the computer, a backslash, the channel name (*ao* for analog output, *ai* for analog input, or *port* for digital input or output), and finally the channel number desired. For example, the string *dev0/ai3* would be used for an analog input on analog input line 3. Any number of channels can be added to a task by stringing them in series.
3. DAQmxBase Start Task: requires a task input. Presumably this VI enables hardware to begin receiving or sending data.
4. DAQmxBase Read/Write: this VI differs based on the type of I/O being performed. This VI requires array input for output tasks. Even if the sample is a single value (e.g. write 3.4 volts to AO1), it must be in an array object (of size 1 in this case). For input tasks, the VI outputs an array containing a sample for each channel in the task. This VI can (and typically will) be called many times within the execution of the program.

5. DAQmxBase End Task: requires a task input and stops the task. This means no more data can be taken from this task until it is restarted. Typically this is done once at the end of the program.
6. DAQmxBase Clear Task: clears the task from memory. End Task and Clear Task must be completed or else the program will not function properly the next time it is run. If the program is halted before End Task and Clear Task run for all tasks in memory, the card must be reset (DAQmxBase Reset Device) or LabVIEW closed and reopened.

D.3 Analog Input Monitor

The first and simplest program in this suite of acquisition and control software is *SimpleAIMonitor(Scopelike).vi*. This program allows the user to specify an analog input (AI) channel to monitor in graphical format, similar to an oscilloscope. It is helpful for ensuring the analog input connections to the computer are correct and making qualitative observations of the output of a photodetector, for example. The AI data collection program described later in section D.4 does not have a graphical display of the inputs it is collecting, as LabVIEW is system resource intensive and any input or output has the potential to slow down the program and cause missed samples. *SimpleAIMonitor(Scopelike).vi* also allows the user to specify an analog output (AO) channel and value to send to that channel. This has been used to set the laser PZT to a specified value to then monitor the analog input from a photodetector on the output of the Fabry-Perot ring cavity. Once it appeared that the input and output were operated as expected, the data collection program could be run.

D.4 Analog Data Collection with Smooth AO Scanning

The motive behind the program *LaserSmoothScanv2.1.vi* was to create a program that could smoothly scan the laser over a specified frequency range (by outputting a voltage through an AO channel to the laser PZT), pausing to collect data from the differential amplifier (which measures the experimental signal). The smooth scanning is needed so that no large jumps in frequency are experienced that would throw the ring cavity out of lock. The program was generalized to take data from up to four independent analog inputs so that other signals of interest could be recorded at the same time as the atomic scan data. An example would be the output from an external Fabry-Perot cavity used to calibrate the frequency of the scans as explained in chapter 5 and appendix C. This program could also take data in an experiment that does not require a control element. While the user of this program will not need to know the details of its operation, anyone wishing to augment or adapt this software will find the general program flow useful (reference figure D.2 for the user interface):

1. Initialize both analog outputs (AO0, AO1) to zero volts.
2. Loop until user selects Begin Scan or Stop. The user can input all desired values at this time. If user selects Stop, terminate the program.
3. Create a task with up to four analog input channels specified by Channel In 1 → 4. Create an analog output task with the channel specified by Channel Out.
4. Start the task. Smoothly scan the analog voltage from zero to Start Voltage Out. The smooth scanning is done by a subVI *AOSmoothStepperv1.vi* which requires inputs for the previous voltage out, the next voltage out, the time it should take to step one volt (calculated from Stepping Time) and the analog output task to write. The VI outputs an analog voltage in incremental steps at the resolution of the DAC (16 bits) until it reaches the finally next voltage out.
5. Perform the scan. Take analog samples at the rate specified by Sample Rate until Number of Samples / Voltage Interval is reached. Concatenate the values to a string in the form (Voltage Out{tab}Voltage In 1{tab}Voltage In 2{tab}Voltage In 3{tab}Voltage In 4{tab}). Smoothly scan to the next analog output value (dictated by Voltage Out Step). Take samples, and repeat until End Voltage Out is reached.
6. Create an output file string by concatenating the header information to the data collected (example header file can be found in section C.1). Prompt the user for a file name to write and then write the entire output string.
7. Go to step 1.

D.5 Stepper Motor Control

The latest program in this suite is intended to be a subVI (*stepper test.vi*) called by a more comprehensive program in the future. It controls a stepper motor mounted in the atomic beam apparatus that can be used to block and unblock the atomic beam. The stepper motor is connected to a power supply and control box that accepts two BNC inputs: **step** and **direction**. Both are TTL digital inputs. The motor steps when the **step** input goes from low to high. The step direction is controlled by the logic state of **direction**: logic low is clockwise, high is counterclockwise. This VI takes three inputs: direction, steps, and operation time (the time the program should take to make all the specified steps). The motor (Superior Electric Slo-Syn Type KML093S07) takes 400 steps per revolution.

Laser Smooth Scanner Version 2
Majumder Lab

Number of Samples / Voltage Interval	Stepping Time (Seconds)	Sample Rate (Samples/Second)	Start Voltage Out	End Voltage Out
<input type="text" value="1000"/>	<input type="text" value="1"/>	<input type="text" value="1000"/>	<input type="text" value="-5"/>	<input type="text" value="5"/>

Channel Out (e.g. ao0)			Voltage Out Step	
<input type="text" value="ao0"/>			<input type="text" value="0.1"/>	

Channel In 1(e.g. ai0)	Ch1 Enable	Ch1 Name	Voltage In 1 Reading	
<input type="text" value="ai0"/>	<input checked="" type="checkbox"/>	<input type="text" value="Voltage In 1"/>	<input type="text" value="0"/>	
Channel In 2	Ch2 Enable	Ch2 Name	Voltage In 2 Reading	Voltage Out
<input type="text" value="ai1"/>	<input checked="" type="checkbox"/>	<input type="text" value="Voltage In 2"/>	<input type="text" value="0"/>	<input type="text" value="0"/>
Channel In 3	Ch3 Enable	Ch3 Name	Voltage In 3 Reading	Sample Number
<input type="text" value="ai2"/>	<input checked="" type="checkbox"/>	<input type="text" value="Voltage In 3"/>	<input type="text" value="0"/>	<input type="text" value="0"/>
Channel In 4	Ch4 Enable	Ch4Name	Voltage In 4 Reading	
<input type="text" value="ai3"/>	<input checked="" type="checkbox"/>	<input type="text" value="Voltage In 4"/>	<input type="text" value="0"/>	

Optional File Header Comment

Begin Scan

STOP

Laser Smooth Scanner v. 2 (Written Fall 2006 T. Schneider – 07tes@williams.edu):

1. Run the program
2. All Analog Output (AO) Channels are set to zero.
3. Set initial values and click "Begin Scan":
 - a. Smoothly scans the voltage on the selected AO channel (ao0 or ao1) to the Start Voltage Out
 - b. When the AO reaches Start Voltage Out, the Selected Number of Samples / Voltage Interval is taken at the Sample Rate from Channel In (any channel from ai0-ai7).
 - c. Voltage Out Step is added to the current AO voltage and smoothly transitioned to.
 - d. Data is taken again. c & d repeat until AO voltage equals End Voltage Out. Stepping will not exceed End Voltage Out, but it might not reach it if Start-End / Step is not an integer.
 - e. Channel Out is set to zero again (smoothly from End Voltage Out)
 - f. Data is saved to a new file selected by the user. If you cancel this dialog, data is lost
4. Repeat scanning as desired. When finished hit the Stop button. Stop is only functional before a scan is in progress.

History:

v2. – Added ability to monitor 4 input channels instead of 1 or 2 and to enable / disable use of these extra channels

Figure D.2: Front panel (user interface) of the *LaserSmoothScanv2.1.vi* smooth scanning data collection routine.

D.6 Oscilloscope Networking

The Tektronix 3014B color oscilloscope employed for various tasks has a waveform memory that can be written to 3.5 inch diskettes. The G4 macintosh does not have such a diskette drive, making it difficult to take data from the oscilloscope (waveforms or settings) and store it. The oscilloscope has a network card with a standard port for RJ-45 cable. Working with the Williams College Networks and Systems employee Todd Gould, it was possible to configure the oscilloscope to work like a computer on the FacStaff (Faculty and Staff) VLAN portion of the network that the G4 macintosh is also configured to work with. Other VLANs (virtual local area networks) did not work. The oscilloscope was given the network name *majumde_scope* and internet protocol (IP) address *137.165.203.182* in subnet *255.255.240.0*. The oscilloscope control software can be accessed by opening a standard web browser to the oscilloscope's IP address (*http://137.165.203.182*). From here, it is possible to download data from the scope, as well as control and monitor any of the functions accessible from the physical buttons.

Bibliography

- [Bru05] Colin D. Bruzewicz, *Phase Shift Spectroscopy in the Study of the $6P_{1/2} \rightarrow 6P_{3/2}$ Transition in a Thallium Atomic Beam* Bachelor's Thesis, Williams College (2005).
- [But06] David L. Butts, *Differential Phase Shift Spectroscopy of the $6P_{1/2} \rightarrow 6P_{3/2}$ 1283 nm Transition in Atomic Thallium* Bachelor's Thesis, Williams College (2006).
- [Dor02] S. Charles Doret, *A Precise Measurement of the Stark Shift in the Thallium $6P_{1/2} \rightarrow 7S_{1/2}$ 378 nm Transition* Bachelor's Thesis, Williams College (2002).
- [Fow75] Grant R. Fowles, *Introduction to Modern Optics* Mineola, NY: Dover Publications (1975).
- [Gri99] David J. Griffiths, *Introduction to Electrodynamics* Upper Saddle River, NJ: Prentice-Hall (1999).
- [HH89] Paul Horowitz, Winfield Hill, *The Art of Electronics, Second Edition* Cambridge, UK: Cambridge University Press (1989).
- [KBUM05] J.A. Kerckhoff, C.D. Bruzewicz, R. Uhl, and P.K. Majumder, "A frequency stabilization method for diode lasers utilizing low-field Faraday polarimetry", *Rev. Sci. Instrum.* 76, 093108 (2005).
- [Ker05] Joseph A. Kerckhoff, *Towards the Measurement of a T-odd P-even Interaction in the $6P_{1/2} \rightarrow 6P_{3/2}$ 1283nm Transition in Atomic Thallium* Bachelor's Thesis, Williams College (2005).
- [Koz89] M.G. Kozlov, S.G. Persev, "The Possibility to Study the Break of Time-Reversal Invariance in Atoms" *Physics Letters* 142A, 233 (1989).
- [LY56] T.D. Lee, and C.N. Yang, "Question of Parity Conservation in Weak Interactions", *Phys. Rev.* 106, 1371 (1956).
- [Nat05] National Instruments, "M Series Help" Document 371022E-01 (2005).

- [Sim07] Owen C. Simpson, *Atomic Spectroscopy in Thallium and Indium Using Frequency Modulation* Bachelor's Thesis, Williams College (2007).
- [SJSC06] M.S. Safronova, W.R. Johnson, U.I. Safronova, and T.E. Cowan, "Relativistic many-body calculations of the Stark-induced amplitude of the $6P_{1/2} \rightarrow 7S_{1/2}$ transition in thallium," *Phys. Rev. A* 74, 022504 (2006).
- [Str07] Jared H. Strait, *Vapor Cell Spectroscopy of Indium Using a 410 nm Diode Laser System* Bachelor's Thesis, Williams College (2007).
- [VMM95] P. Vetter, D.M. Meekhof, P.K. Majumder, S.K. Lamoreaux, and E.N. Fortson, "Precise test of electroweak theory from a measurement of parity nonconservation in atomic thallium," *Phys. Rev. Lett.* 74, 2658 (1995)
- [WA57] C.S. Wu, E. Ambler et al. "Experimental Test of Parity Conservation in Beta Decay." *Phys. Rev.* 105, 1413 (1957).